Supplementary Information for: Managing intermittency of renewable power in sustainable production of methanol, coupled with direct air capture

George J. Fulham[1*], Paula V. Mendoza-Moreno[1] and Ewa J. Marek[1*]

[1]Department of Chemical Engineering and Biotechnology, University of Cambridge, Philippa Fawcett Drive, Cambridge, CB3 0AS, Cambridgeshire, United Kingdom.

*Corresponding author(s). E-mail(s): gf325@cam.ac.uk; ejm94@cam.ac.uk; Contributing authors: pvm21@cam.ac.uk;

1 An overview of salient prior studies

Here, we provide a summary of pertinent prior work concerning: (1) Power-to-Methanol; (2) the dynamic operation of other PtX processes; (3) renewably powered DAC. The studies are grouped by their area of focus and ordered by publication date.

1.1 Power-to-Methanol (PtM)

Authors and date	Overview of modelling	Key findings
Fogel *et al.* (2024) [1]	• PtM system using tubular high-temperature solid oxide electrolyser cells (SOEC) for H_2 production, for reaction with CO_2 in a single MeOH synthesis reactor followed by downstream separation. • Detailed modelling of transport phenomena within the tubular SOEC, considering the effects of current density and the transient behaviour during step changes in applied voltage.	• Overall PtM energy efficiency between 38% and 56% depending on current density within the SOEC. • Waste heat from SOEC able to cover thermal requirements of the MeOH synthesis section. • The entire PtM system reaches new steady state around 1 h after step change in cell voltage of around 5%.
Van Antwerpen *et al.* (2023) [2]	• PtM at sites across Australia (and one site each in Germany and Chile), with power from hybridisation of wind and solar PV. • Considers taking CO_2 from either industrial sources or DAC. • H_2 from PEM electrolyser stacks, with balancing storage in either pressurised tanks/pipes or salt caverns. • Operates plant with a single reactor under 4 different regimes depending upon available power: (1) full capacity operation, filling storage with surplus; (2) scaled-down throughput to match available power; (3) use of reserve storage to supplement plant operation; (4) plant downtime during low power if storage is empty.	• Price of MeOH ranges from $900 – 1,300/t_{MeOH}$ if using industrial flue gas, rising to $1,140-1,570/t_{MeOH}$ if converting CO_2 from DAC. • The variation in MeOH selling price is predominantly driven by differences between candidate sites for renewable power installation. • Increased proportion of solar in the hybrid mix from 50% to 90% causes a roughly 20% increase in MeOH selling price. • Excessive oversizing of renewable power capacity (*i.e.* reducing drastically the reserve storage) does not improve selling price.
Zheng *et al.* (2023) [3]	• Power-to-Methanol-to-Power system for balancing intermittent solar PV power. • SOEC for syngas production from CO_2 and H_2O during the day, with thermal energy storage for heating of the SOEC. • Outlet composition of syngas varies with solar PV generation and is fed to MeOH synthesis, causing MeOH yield to vary dynamically. • MeOH is stored in balancing tanks to later pass through solid oxide fuel cell for power generation. • Source of CO_2 is not considered, nor are the life cycle emissions.	• Approximately 75% of CAPEX from solid oxide cells, and around 15% from PV plant. • Cost of MeOH is $1,490/t_{MeOH}$ when operating the SOEC at 973 K, falling to $490/t_{MeOH}$ if the SOEC is at 1073 K.

Moioli and Schildhauer (2023) [4]	• PtM from biogas with a limited consideration of flexible operation. • Only data from Switzerland are used in estimating a breakdown of operating hours between: (1) biogas upgrading to MeOH with green H_2 (during available power), (2) biogas steam reforming (when power is unavailable). • Sensitivity analysis performed on electricity price under conditions of abundance and scarcity. • Simplified capital cost determinations, only for the major equipment.	• Methanol production from biogas more cost-effective than methane under time-varying price of renewable power.
Sollai *et al.* (2023) [5]	• Considers amine scrubber for CO_2 capture from flue gas, with H_2 from PEM electrolysis. • Some reserve storage of H_2 and CO_2, but no consideration of the time-variability of power. • Cost analysis includes an assumed carbon credit of $85/t_{CO_2}$.	• Levelised methanol cost is $1,030/t_{MeOH}$ under base case. • The selling price is highly sensitive to the plant capacity factor, rising to around $1,500/t_{MeOH}$ for a plant capacity factor of $\sim 60\%$.
Zheng *et al.* (2022) [6]	• Consideration of PtM connected to grid power, focusing on an example of grid-integrated wind power in Denmark. • CO_2 sourced from biogas, and H_2 from alkaline electrolyser. MeOH synthesis within a single Lurgi methanol reactor, capable of ramping from 10-15% load to full capacity within minutes. • Use of real-world wind data, at a single site, for prediction of electricity purchase price from the local grid for PtM. • Dynamic optimisation of plant operating capacity (max. 2,000 kg_{MeOH}/h) according to predicted electricity price. • 200 kg H_2 buffer tank used to support dynamic operation. • Life cycle inventory of wind turbines incorporated into the analysis (7.3 kg_{CO2eq}/MWh$_e$).	• Cost of MeOH production ranges from €580-1150/t_{MeOH}, for predicted electricity prices in the range €32-65/MWh$_e$. • Estimated process emissions of around 800 kg_{CO2eq}/t_{MeOH}.
Cui *et al.* (2022) [7]	• Developed a dynamic process model for MeOH synthesis and distillation, taking in pure feed streams of H_2 and CO_2. • The model is subjected to ramping between operating loads, and is then used to train a surrogate model with which to simulate MeOH synthesis and distillation under time-varying load across 108 h. The variable load modelling considers an arbitrary load profile, rather than real-world weather data. • Analysis focuses on the effect of dynamic operation upon process efficiency, and so does not evaluate the cost or environmental impact of methanol production.	• Combined system is able to achieve ramp between 50% and 100% load in 1 h, with energy efficiency fully settling after 2 h. • MeOH synthesis and distillation is 88% energy efficient at full-load, and rises to 90% at half-load. • The system is able to track an operating load profile between 50% and 100% across 108 h. However, the behaviour of the system at below half-load is unknown.

Chen *et al.* (2021) [8]	• PtM using CO_2 captured from flue gas, which is considered within the system boundary. • Electricity is predominantly from wind and solar PV power, with scenarios to consider varying the support from (1) reserve storage of H_2 *vs* (2) connection to dispatchable grid electricity. • Matches the total time-averaged solar and wind power to the total load of the PtM, which is assumed to run at steady state. Analysis also considers deliberately over-sizing the installed renewable capacity to reduce reliance on reserve storage or grid electricity. • When not reliant on dispatchable grid power (*i.e.* wholly dependent on renewable power), the plant uses reserve storage of H_2, which is also run through fuel cells to provide reserve electricity. • Analysis considers two sites: Kramer Junction (US) and Norderney (Germany). • Economic analysis optimises the reliance on purchase of grid power and reserve storage. • Storage levels of H_2 modelled across a year for each location.	• Optimised selling price of between \$1,400 and 1,500/t_{MeOH}. • Kramer junction requires a roughly 90% over-sizing of the renewable power to operate continuously at steady-state, using only reserve storage; whereas, Norderney requires only a 16% over-sizing of the wind and solar nameplate capacity. • 5 tonnes of reserve storage H_2 at Norderney, rising to 15 tonnes at Kramer Junction. However, this storage capacity does not prevent the storage running empty for around 1 to 3% of the year. • Most economical solution for Kramer Junction requires drawing approximately 20% of power from the grid, leading to a net positive carbon intensity of 210 kg_{CO2eq}/t_{MeOH}. • At Norderney, the most economical solution requires only around 8% power from the dispatchable grid, and has a net negative carbon intensity of -770 kg_{CO2eq}/t_{MeOH}.
Bos *et al.* (2020) [9]	• DAC-PtM using solid amine for CO_2 capture, and PEM electrolysis for H_2 production. • Annual production of 65,000 tonnes of MeOH. • MeOH synthesis performed within novel Liquid-Out Gas-In Concept (LOGIC) reactor, where the methanol and water are flashed out *in situ* using a temperature gradient within the reactor. • Power for process entirely from a wind farm, assuming 100 MW of installed wind power was available to enable 8,000 continuous hours of operation. • No dynamic operation or reserve storage included in modelling or cost estimates. • Straightforward costing of unit operations based on process flow diagram.	• Overall PtM energy efficiency of between 49 and 53%. • Total CAPEX of €200 million for the plant, excluding the wind farm installation cost (€300 million) • Around 45% of process CAPEX arising from PEM electrolysis. • Estimated MeOH cost of around €800/t_{MeOH}, including the wind farm installation cost.
Daggash *et al.* (2018) [10]	• DAC-PtM using potassium hydroxide for CO_2 capture, and alkaline electrolysers for H_2 production. • All the required power is supplied through the purchase of curtailed renewable power within the UK grid, at \$55/MWh. • The availability of curtailed power is estimated for an optimised future grid scenario, with up to 60% penetration of intermittent renewable sources and a mixture of balancing storage, including pumped hydro and batteries.	• At most, the availability of curtailed renewable power will only be 2.5% of the installed capacity. • The selling price of methanol is \$960/t_{MeOH}, requiring a carbon subsidy of \$280/t_{CO2} to achieve parity with current MeOH selling prices. • Substituting DAC for post-combustion carbon capture, and electrolysis for steam methane reforming, the methanol selling price falls to \$523/t_{MeOH}, still above current MeOH selling prices.

1.2 Direct air capture (DAC) with renewable power

Authors and date	Overview of modelling	Key findings
Gutsch and Leker (2024) [11]	• DAC using sorbents, reliant solely on PV power with batteries for reserve storage. • Primarily considers operations in Nevada, although Germany and Namibia are also investigated. • Analysis primarily considers changing the ratio between installed PV capacity and battery storage to find the most cost-effective option. • Heat pumps used to provide the desorption heat. • Life cycle assessment performed to determine the net CO_2 capture by DAC, and hence the effective cost of CO_2 capture.	• The effective cost of DAC, in Nevada, is optimised for a 300 MW PV farm with 100 MWh battery storage at \$890 per tonne of net CO_2 capture.
Breyer *et al.* (2020) [12]	• Forecasts future energy mixes, including both PV and wind, for powering DAC using solid sorbents and heat pump technology. • Utilises real-world weather data focusing on the Maghreb region in the study. • Modelling predicts the feed-in of PV and wind power to the grid by 2050, and hence, the future purchase cost of electricity.	• Levelised cost of €105 per tonne of CO_2 predicted by 2030 in the considered Maghreb region, falling to a predicted €55 per tonne by 2050.
Daggash *et al.* (2018) [10]	• DAC using potassium hydroxide, with all electricity from the curtailment of UK grid-integrated renewable power source, at \$55/MWh.	• Cost of capture between \$430 and \$660 per tonne of CO_2 captured.

1.3 Power-to-Liquid (PtL)

Authors and date	Overview of modelling	Key findings
Pratschner *et al.* (2024) [13]	• Compares grid-based and off-grid PtL plants performing Fischer Tropsch (FT) synthesis. • Renewable power sourced from either wind, PV, geothermal, and hydro power; however, the off-grid scenarios consider only the full-load hours with each power source – *i.e.* neither dynamic operation nor reserve storage are considered. • The capital costs of erecting renewable power sources for off-grid power provision are not directly taken as part of the PtL capital expenditure.	• Around 90% of selling price arises from electricity provision. • Off-grid PtL substantially cheaper than grid-powered PtL: 1.28 to 2.40 €/kg *vs* 2.52 to 4.56 €/kg.
Loewert *et al.* (2020) [14]	• Considers Fischer-Tropsch synthesis from syngas under a dynamic PV profile. • Experimental FT results in a micro-structured reactor are coupled with an experimental PV profile over a single day to model the effect of dynamic operation (including changing syngas composition and reactor temperature) upon the yield and product composition. • Catalyst stability is also probed experimentally.	• Model suggests that dynamic operation is feasible within a micro-structured reactor. • Reactor can tolerate around 50% fluctuations in throughput. • Catalyst shows deactivation over 70 days of operation, with CO conversion falling from ∼60% to ∼45%.

Shirazi *et al.* (2019) [15]	• FT synthesis driven by concentrated solar power. • Applies a perfect one-day ahead scheduler, supplied with weather data for Geraldton in Australia, to control the solar-driven gasification of biomass which feeds syngas to the FT synthesis. The FT is modelled for a single, large reactor. • Modelling of predicted storage level across a day and the annual consumption of algal biomass. • Straightforward determination of capital and operating expenditure.	• The cost of fuel products was very sensitive to the ramp rate of the single, large reactor.

1.4 Power-to-Gas (PtG)

Authors and date	Overview of modelling	Key findings
Giglio *et al.* (2021) [16]	• Power-to-Gas (PtG), with Sabatier reaction between CO_2 and H_2, focusing on dynamic operation of methanation reactor. The sourcing of CO_2 and H_2 does not form part of the model. • One-dimensional transport phenomena model for shell-and-tube reactor configuration during start-up from hot standby ($250°C$), and during load adjustment from 100% down to 80%.	• Reactors reach steady state within 1 min of start-up from hot standby mode or load adjustment.
Gorre *et al.* (2020) [17]	• Dynamic operation of PtG, decoupling H_2 production from the methanation subsystem through intermediate H_2 storage in tanks, which is only at between 10 and 30 bar. • Process uses surplus renewable power from grid-integrated wind or solar PV, taking data only from Switzerland and Germany. • Considers generic CO_2 source without intermediate storage. • Single reactor used, which is held in standby mode when not in use (achieved by flushing with H_2 and reducing operating temperature). Losses of H_2 during idling and restart procedures are considered. • The pressure of H_2 within the balance tank (being filled directly from an alkaline electrolyser) determines whether the reactor begins to operate — *i.e.* stored reserves must be above a threshold of 18 bar before the reactor can operate. • Assumes that reactor is ramped at 3% per minute, allowing for multiple start-ups and shut-downs per day. • Process investigated through Monte Carlo sensitivity analysis on key CAPEX items and the duration of standby and reactor restart. • Modelling also considers a scenario in which all H_2 must be converted, and another which allows for some H_2 to be discarded to aid dynamic operation.	• The size of H_2 reserve storage is optimised to minimise the resulting cost of methane. • Electrolyser represents *ca.* 60% of plant CAPEX, which excludes the capital cost of wind and solar PV farm. • Number of operational hours per month evaluated across a given year for wind and solar PV power. • Reactor is started-up and shut-down as many as 500 times per annum.

1.5 Power-to-Ammonia (PtA)

Authors and date	Overview of modelling	Key findings
Mock *et al.* (2023) [18]	• NH_3 synthesis in a cascade of dynamic tubular reactors. • Predominantly wind power, with grid connection for stand-by operation during low wind power. • Buffer storage of H_2, from PEM electrolysis, in tanks. A constant supply of N_2 from pressure swing adsorption (PSA) is assumed.	• Dynamic modelling of reactor cascade shows ability to ramp reactors at 200% of nominal load per hour.
Verleysen *et al.* (2023) [19]	• Dynamic operation considered at the minute scale over a 3 h period, using a stochastic model of wind power fluctuations. • Deliberately neglects any constraints on achievable reactor loads. • H_2 from PEM electrolysis and N_2 from PSA, with an optimised portion of each gas diverted to buffering storage. • Considered flexibility of system as the ratio of maximum to minimum instantaneous NH_3 production rates. To appraise system resilience, changes to the reactor operating temperature were modelled across the 3 h.	• Clear trade off observed between flexibility and resilience – i.e. allowing ammonia production to vary more widely lead to sharper fluctuations in operating temperature. • Higher flexibility required larger bypass flowrate of H_2 to reserve storage.
Ishaq and Dincer (2021) [20]	• PtA integrated with solar thermal power (heliostat generating steam for a Rankine cycle). H_2 from PEM electrolysis and N_2 from PSA, with NH_3 produced in a cascade of packed bed reactors. • Focuses on Toronto, Canada as the candidate location, and considers just one average day per month across a single year. • Model does not consider dynamic operation, but instead analyses the system performance for the chosen day in each month across the year.	• Process efficiencies between 12% and 30% across the year.
Ikäheimo *et al.* (2018) [21]	• Considered an electricity generation mix comprising both renewables and thermal plants. • Studied locations across the Nordic and Baltic regions, as well as Poland and Germany. • H_2 from PEM electrolysis and N_2 from cryogenic distillation of air • Compressed H_2 storage considered for balancing, and ammonia liquified for intermediate storage after production. • Modelling considered the transmission of electricity between studied locations, and dynamic changes in curtailment of renewables, to estimate cost of ammonia production.	• Wholly renewable NH_3 can achieve parity with NH_3 from fossil fuels. • Reserve storage size was equivalent to 2.1% of annual electricity demand for the process.
Cheema and Krewer (2018) [22]	• Investigation of operating envelope of Haber-Bosch process during dynamic operation. • H_2 and N_2 taken from reserve storage tanks and fed into the NH_3 synthesis loop comprising a cascade of three reactors with inter-cooling. • Dynamic thermal and kinetic modelling of the reactor subjected to variations of the inlet flow of reactants.	• Around 60% flexibility in H_2 inlet flowrate while still achieving stable operation. • Possible to raise production by around 25% above nominal load and decrease by 75%.

2 Modelling the intermittency of wind power

The results presented within the main body of the paper consider situating a wind farm at either an in-land onshore location, or offshore out at sea. A third option is for an onshore wind farm to be situated in a coastal location (*i.e.* less than 20 km from the sea), results for which were also collected. Thirty potential locations were selected for each option. The onshore and offshore locations considered are tabulated in **Tab. 1**. The offshore locations are listed in terms of the body of water in which the farm would be located (*e.g.* North Sea), and the country to whom the section of water belongs (*e.g.* Great Britain).The additional coastal locations are provided in **Tab. 2**.

Table 1: A list of the 60 locations, both onshore and offshore, considered in the analysis of wind power generation in the years 2016 to 2020. The offshore locations are listed in terms of the body of water in which the farm would be located (*e.g.* North Sea), and the country to whom the section of water belongs (*e.g.* Great Britain).

Onshore			Offshore		
Region	**Country**	**Location**	**Region**	**Country**	**Location**
Africa	Algeria	Adrar	Africa	Djibouti	Red Sea
Africa	Botswana	Ghanzi	Africa	Egypt	Red Sea
Africa	Chad	Iriba	Africa	Madagascar	Indian Ocean
Africa	Egypt	Baris	Africa	Mauritania	North Atlantic Ocean
Africa	Senegal	Tambacounda	Africa	Namibia	South Atlantic Ocean
Africa	Zambia	Ndola	Asia	Azerbaijan	Caspian Sea
Asia	China	Yumen	Asia	China	Yellow Sea
Asia	China	Changchun	Asia	India	Laccadive Sea
Asia	Kazakhstan	Kyzylorda	Asia	Japan	East Sea
Asia	Mongolia	Mandalgobi	Asia	Oman	Arabian Sea
Asia	Saudi Arabia	Medina	Asia	Taiwan	Philippine Sea
Asia	Sri Lanka	Polonnaruwa	Asia	Vietnam	South China Sea
Asia	Uzbekistan	Bukhara	Europe	Denmark	Skagerrak
Europe	Denmark	Viborg	Europe	France	Mediterranean Sea
Europe	Finland	Kuopio	Europe	Great Britain	North Sea
Europe	France	Amiens	Europe	Great Britain	Irish Sea
Europe	Germany	Dresden	Europe	Greece	Aegean Sea
Europe	Great Britain	Kelso	Europe	Ireland	North Atlantic Ocean
Europe	Italy	Lucera	Europe	Norway	Norweigan Sea
Europe	Netherlands	Enschede	N. America	Canada	North Atlantic Ocean
N. America	Canada	Calgary	N. America	Mexico	Gulf of Mexico
N. America	USA	Wichita	N. America	USA	North Pacific Ocean
N. America	USA	West Bend	N. America	USA	Bering Sea
N. America	USA	Austin	N. America	USA	Sargasso Sea
N. America	USA	Mankato	S. America	Argentina	South Atlantic Ocean
S. America	Argentina	Rosario	S. America	Chile	South Pacific Ocean
S. America	Bolivia	Santa Cruz	S. America	Peru	South Pacific Ocean
S. America	Brazil	Itaueira	S. America	Venezuela	Caribbean Sea
S. America	Chile	Osorno	Oceania	Australia	Indian Ocean
Oceania	Australia	Alice Springs	Oceania	New Zealand	Tasman Sea

Table 2: A list of the 30 additional coastal locations considered in the analysis of wind power generation in the years 2016 to 2020.

Coastal Onshore		
Region	**Country**	**Location**
Africa	Kenya	Mombasa
Africa	Morocco	Tarfaya
Africa	Mozambique	Quelimane
Africa	Senegal	Rufisque
Africa	South Africa	Port Elizabeth
Asia	Azerbaijan	Sumgayit
Asia	China	Dalian
Asia	China	Xiamen
Asia	India	Kanyakumari
Asia	Japan	Sasebo
Asia	Saudi Arabia	Dammam
Asia	South Korea	Busan
Asia	Vietnam	Phan Rang
Europe	Great Britain	Aberdeen
Europe	Iceland	Keflavik
Europe	Poland	Gdansk
Europe	Romania	Constanta
Europe	Spain	Bilbao
Europe	Sweden	Gothenburg
N. America	Canada	Salluit
N. America	Mexico	Salina Cruz
N. America	Panama	Arraijan
N. America	Trinidad and Tobago	Marabella
N. America	USA	Halifax
N. America	USA	Providence
S. America	Brazil	Porto Alegre
S. America	Falkland Islands	Stanley
S. America	Uruguay	Maldonado
Oceania	Australia	Port Lincoln
Oceania	New Zealand	Dunedin

The collected data were processed to yield the daily average power output at each location. The annual capacity factor, for each location in a given year, was then calculated according to **Eq. 1**.

$$\overline{CF}_{j,k} = \frac{\sum_{i=1}^{365} P_{i,j,k}}{365 \times 100} \ , \tag{1}$$

where $\overline{CF}_{j,k}$ is the annual capacity factor at the jth location ($j = 1$ to 30) in the kth year ($k = 2016$ to 2020), and $P_{i,j,k}$ is the daily average power output from the wind farm on the ith day ($i = 1$ to 365). The 100 refers to the nameplate power used in gathering the data. A daily capacity factor, $CF_{i,j,k}$, was also defined according to **Eq. 2**.

$$CF_{i,j,k} = \frac{P_{i,j,k}}{100} \ . \tag{2}$$

Example plots are given in **Figs. 1**, **2**, and **3** for the variation of $CF_{i,j,k}$ across a year at various in-land and coastal locations, respectively. The locations shown in **Figs. 1**, **2**, and **3**, and the years they span, were selected at random for illustrative purposes. Comparison of **Figs. 1** and **2** illustrates the significant difference in the extent of power fluctuations, when comparing in-land onshore and offshore locations. The offshore locations attain daily capacity factors close to 1 (*i.e.* near their maximum possible power output) more frequently than in-land locations, leading to on-average higher values of

$\overline{CF}_{j,k}$ for offshore *versus* in-land locations. However, the offshore sites also exhibit more drastic variations in daily power generation than wind farms located in-land, as seen in **Fig. 1**, thus, necessitating greater reliance on reserve storage. Inspection of the coastal wind farm sites in **Fig. 3** shows that the coastal in-land sites experience larger fluctuations than in-land locations, similar to the offshore locations in **Fig. 1**. However, the annual capacity factors tend to be lower for coastal sites compared to offshore sites, as the wind speeds are lower at coastal onshore sites than offshore at sea.
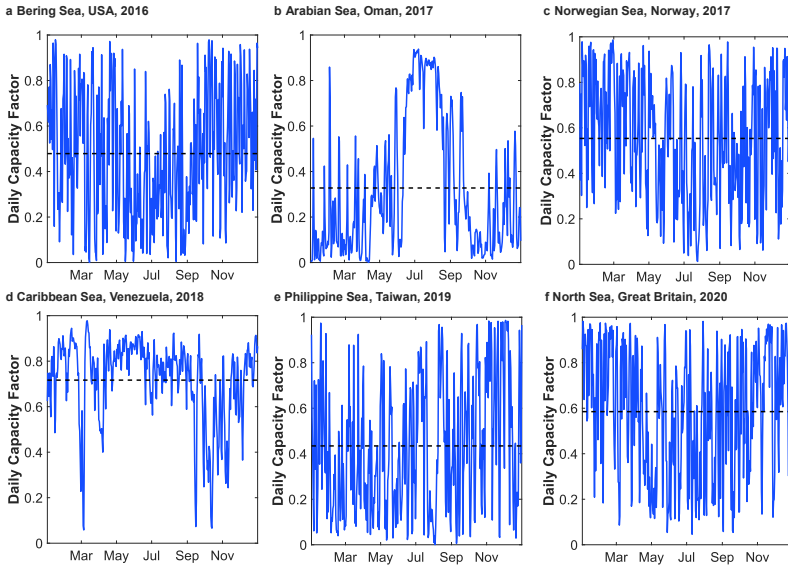

Fig. 1: The daily CF for six offshore locations across a given year: **a** Bering Sea, USA, 2016; **b** Arabian Sea, Oman, 2017; **c** Norweigan Sea, Norway, 2017; **d** Caribbean Sea, Venezuela, 2018; **e** Philippine Sea, Taiwan, 2019; **f** North Sea, Great Britain, 2020. The annual average $\overline{CF}$ is indicated by the black hatched horizontal line.
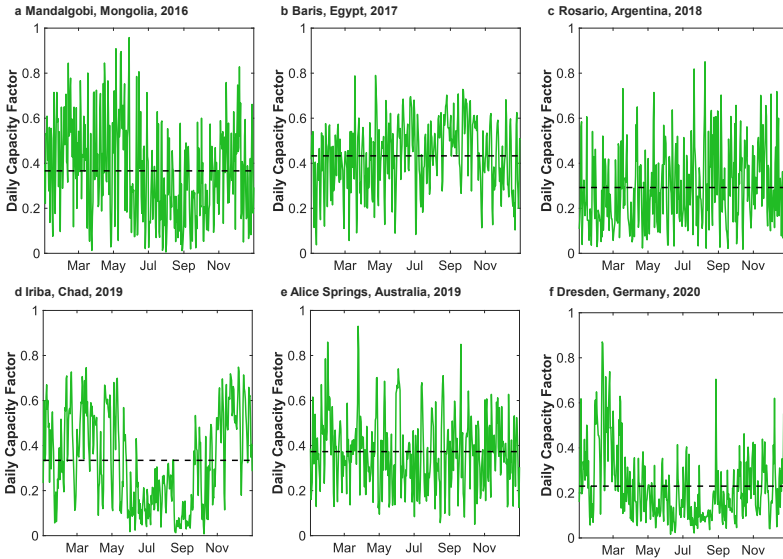
Fig. 2: The daily CF for six in-land onshore locations across a given year: **a** Mandalgobi, Mongolia, 2016; **b** Baris, Egypt, 2017; **c** Rosario, Argentina, 2018; **d** Iriba, Chad, 2019; **e** Alice Springs, Australia, 2019; **f** Dresden, Germany, 2020. The annual average $\overline{CF}$ is indicated by the black hatched horizontal line.
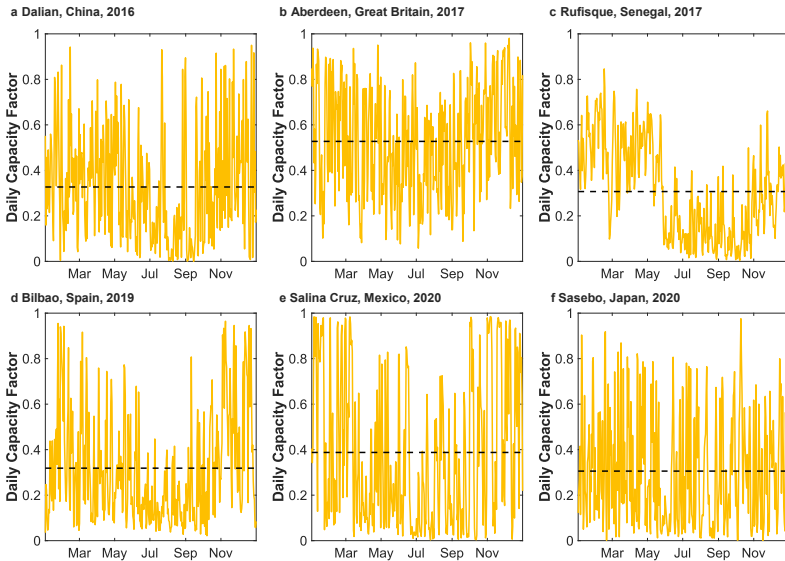

Fig. 3: The daily CF for six coastal onshore locations across a given year: **a** Dalian, China in 2016; **b** Aberdeen, Great Britain in 2017; **c** Rufisque, Senegal in 2017; **d** Bilbao, Spain in 2018; **e** Salina Cruz, Mexico in 2020; and **f** Sasebo, Japan in 2020. The annual average $\overline{CF}$ is indicated by the black hatched horizontal line.

3 Relating the performance of a wind farm site to the operation of power-to-methanol

The wind farm capacity factor, $\overline{CF}_{j,k}$, was used to estimate the required size of a hypothetical wind farm, for a given year at a given site, to be constructed for PtM, according to **Eq. 3** (as also expressed in **Eq. 1** in the main paper).

$$P_{\text{nameplate}} = \frac{P_{\text{PtM}}}{\overline{CF}_{j,k}} \, , \tag{3}$$

where $P_{\text{nameplate}}$ refers to the nameplate (*i.e.* ideal maximum) power output from the wind farm, and P_{PtM} is the typical power demand of PtM at full production capacity (*i.e.* with all four reactors operational). Hence, the annual average power generation from the wind farm matched the power demand to produce methanol, *via* DAC-PtM, at its intended capacity of 50,000 tonnes per annum. However, the regular drops in power generation below the annual average power output – therefore also below the power requirement for running PtM at full capacity – necessitated reducing the power demand of PtM by taking reactors off-line in order to reduce throughput, and then consuming stored reserves when necessary. The operation Strategies 1 and 2, shown in **Fig. 3**, were used to govern the dynamic operation. Here, we outline the algorithms developed in MatLab for implementing each strategy. In both instances, a comparison was made between the predicted daily capacity factor, $CF_{i,j,k}$, and the annual average for the location, $\overline{CF}_{j,k}$ to determine the correct number of operational reactors on each day, denoted as $n_{i,j,k}$.

3.1 Strategy 1

A summary is given in **Tab. 3** of how the daily number of operational reactors was adjusted according to the daily capacity factor for Strategy 1.

Table 3: The algorithm used to estimate the daily number of operational reactors when operating under Strategy 1.

A.	$CF_{i,j,k} \geq \overline{CF}_{j,k}$	$\to n_{i,j,k} = 4$	Operate all 4 reactors
B.	$\overline{CF}_{j,k} > CF_{i,j,k} \geq 3/4\overline{CF}_{j,k}$	$\to n_{i,j,k} = 3$	Operate 3 reactors
C.	$3/4\,\overline{CF}_{j,k} > CF_{i,j,k} \geq 1/2\overline{CF}_{j,k}$	$\to n_{i,j,k} = 2$	Operate 2 reactors
D.	$1/2\,\overline{CF}_{j,k} > CF_{i,j,k} \geq 1/4\overline{CF}_{j,k}$	$\to n_{i,j,k} = 1$	Operate 1 reactor
E.	$1/4\,\overline{CF}_{j,k} > CF_{i,j,k}$	$\to n_{i,j,k} = 1$	Operate 1 reactor using stored reserves

Having found values of $n_{i,j,k}$ – *i.e.* the predicted number of operational reactors on each day (i) for a given location (j) in a given year (k) – the

plant capacity factor (the ratio of actual annual production against maximum capacity) was estimated as:

$$\overline{CF}_{\text{plant } j,k} = \frac{\sum_{i=1}^{365} n_{i,j,k}}{4 \times 365} \ , \tag{4}$$

where $\overline{CF}_{\text{plant; } j,k}$ is the annual average plant capacity factor for the jth location ($j = 1 \text{ to } 30$) in the kth year ($k = 2016 \text{ to } 2020$). Within scenario A, as defined in **Tab. 3**, the power output exceeds the annual average, and therefore also the power demand of the PtM plant. Thus, the wind farm produces a surplus of power. The size of the surplus in each year and at each location, $S_{j,k}$, was calculated as a fraction of the annual generation according to the conditional summation in **Eq. 5**.

$$S_{j,k} = \frac{\sum_{i=1}^{365} \begin{cases} CF_{i,j,k} - \overline{CF}_{j,k} & \text{if } CF_{i,j,k} > \overline{CF}_{j,k} \\ 0 & \text{if } CF_{i,j,k} \leq \overline{CF}_{j,k} \end{cases}}{365 \times \overline{CF}_{j,k}} \ , \tag{5}$$

where all terms are as previously defined. The calculation was normalised against nameplate power capacity and performed in terms of capacity factor values, as shown in **Eq. 5**.

In addition to surplus power generation above the annual average output, scenarios B to D in **Tab. 3** present an excess of power due to the curtailment of production such that power demand is below availability. For example, if the daily capacity factor is only slightly below the annual average (scenario B), a more than sufficient amount of power is generated to operate at the throughput for three reactors, but insufficient power to operate at full throughput with four reactors. The energy, $E_{j,k}$, available from periods of reduced operation (scenarios B to D as described above) was calculated *via* a conditional summation in **Eq. 6**. As with the surplus, $E_{j,k}$ is expressed as a fraction of the annual electricity generation.

$$E_{j,k} = \frac{\left(\begin{array}{l} \sum\limits_{i=1}^{365} \begin{cases} CF_{i,j,k} - 3/4\,\overline{CF}_{j,k} & \text{if } \overline{CF}_{j,k} > CF_{i,j,k} > 3/4\,\overline{CF}_{j,k} \\ 0 & \text{else} \end{cases} + \\ \sum\limits_{i=1}^{365} \begin{cases} CF_{i,j,k} - 1/2\,\overline{CF}_{j,k} & \text{if } 3/4\,\overline{CF}_{j,k} > CF_{i,j,k} > 1/2\,\overline{CF}_{j,k} \\ 0 & \text{else} \end{cases} + \\ \sum\limits_{i=1}^{365} \begin{cases} CF_{i,j,k} - 1/4\,\overline{CF}_{j,k} & \text{if } 1/2\,\overline{CF}_{j,k} > CF_{i,j,k} > 1/4\,\overline{CF}_{j,k} \\ 0 & \text{else} \end{cases} \end{array} \right)}{365 \times \overline{CF}_{j,k}} \tag{6}$$

Here, we used the available energy given by **Eq. 6** for running DAC and electrolysis, before compressing the gases up to their storage pressures, all in readiness for a period in which the plant then relies upon reserve storage

(scenario E in **Tab. 3**). The sizing of reserve storage at each site for Strategy 1 was determined by finding the maximum number of days on which the DAC-PtM operated in scenario E within a two-month period.

3.2 Strategy 2

When operating under Strategy 2, stored reserves were used to boost the number of operational reactors. A summary is given in **Tab. 4** of how the daily number of operational reactors was adjusted according to the daily capacity factor.

Table 4: The algorithm used to estimate the daily number of operational reactors when operating under Strategy 2.

A.	$CF_{i,j,k} \geq \overline{CF}_{j,k}$	$\rightarrow n_{i,j,k} = 4$	Operate all 4 reactors and fill storage
B.	$\overline{CF}_{j,k} > CF_{i,j,k} \geq 3/4\overline{CF}_{j,k}$	$\rightarrow n_{i,j,k} = 4$	Operate 4 reactors using stored reserves
C.	$3/4\,\overline{CF}_{j,k} > CF_{i,j,k} \geq 1/2\overline{CF}_{j,k}$	$\rightarrow n_{i,j,k} = 3$	Operate 3 reactors using stored reserves
D.	$1/2\,\overline{CF}_{j,k} > CF_{i,j,k} \geq 1/4\overline{CF}_{j,k}$	$\rightarrow n_{i,j,k} = 2$	Operate 2 reactors using stored reserves
E.	$1/4\,\overline{CF}_{j,k} > CF_{i,j,k}$	$\rightarrow n_{i,j,k} = 1$	Operate 1 reactor using stored reserves

The plant capacity factor was then determined using the same **Eq. 4** as for Strategy 1. Under Strategy 2, the filling of storage only occurs when the daily generation exceeded the annual average (*i.e.* scenario A in **Tab. 4**). The energy available for such filling, $F_{j,k}$, is the same as the surplus electricity in Strategy 1, and so was calculated using the same methodology:

$$F_{j,k} = \frac{\sum_{i=1}^{365} \begin{cases} CF_{i,j,k} - \overline{CF}_{j,k} & \text{if } CF_{i,j,k} > \overline{CF}_{j,k} \\ 0 & \text{if } CF_{i,j,k} \leq \overline{CF}_{j,k} \end{cases}}{365 \times \overline{CF}_{j,k}} \,, \tag{7}$$

where all terms are as previously defined. The sizing of reserve storage for Strategy 2 at each site was performed by determining the maximum number of days on which the plant required the use of stored reserves (*i.e.* scenarios B to E in **Tab. 4**) within a two-month period.

4 Best performing locations under Strategies 1 and 2

The results in **Tab. 5** show that some locations (*e.g.* Baris in Egypt) deliver very high plant capacity factors regardless of operating regime; whereas, some sites (*e.g.* Viborg in Denmark) perform markedly better under Strategy 2 than Strategy 1, or *vice versa*.

Table 5: The top 10 considered locations, in terms of plant capacity factor, for the operation of DAC-PtM under either Strategy 1 or 2.

	Onshore				
	Strategy 1			**Strategy 2**	
	Location	$\overline{CF}_{\text{plant}}$	Location		$\overline{CF}_{\text{plant}}$
1	Baris, Egypt	79.5%	Baris, Egypt		90.7%
2	Alice Springs, Australia	75.3%	Alice Springs, Australia		87.7%
3	Adrar, Algeria	74.1%	Medina, Saudi Arabia		85.6%
4	Medina, Saudi Arabia	72.6%	Adrar, Algeria		85.3%
5	Iriba, Chad	72.1%	Viborg, Denmark		83.5%
6	Mandalgobi, Mongolia	71.8%	Kuopio, Finland		83.3%
7	Wichita, USA	70.6%	Rosario, Argentina		83.3%
8	Mankato, USA	70.5%	Mandalgobi, Mongolia		82.8%
9	Rosario, Argentina	70.5%	Wichita, USA		82.1%
10	West Bend, USA	70.4%	Mankato, USA		81.8%

	Offshore				
	Strategy 1			**Strategy 2**	
	Location	$\overline{CF}_{\text{plant}}$	Location		$\overline{CF}_{\text{plant}}$
1	Caribbean Sea, Venezuela	82.8%	Caribbean Sea, Venezuela		91.3%
2	South Pacific Ocean, Chile	77.7%	North Sea, Great Britain		86.5%
3	Tasman Sea, New Zealand	76.9%	Tasman Sea, New Zealand		86.2%
4	North Sea, Great Britain	76.3%	North Atlantic Ocean , Ireland		86.0%
5	North Atlantic Ocean , Ireland	76.2%	South Pacific Ocean, Chile		85.8%
6	North Atlantic Ocean, Mauritania	75.8%	Norwegian Sea, Norway		85.3%
7	North Atlantic Ocean, Canada	74.9%	North Atlantic Ocean, Mauritania		85.1%
8	Norwegian Sea, Norway	74.7%	South Atlantic Ocean, Argentina		85.0%
9	South Atlantic Ocean, Namibia	74.3%	Irish Sea, Great Britain		84.5%
10	Irish Sea, Great Britain	74.1%	North Atlantic Ocean, Canada		84.5%

5 Comparison of the cost of battery storage *versus* compressed gases

The projected capital cost of utility-scale battery storage is forecast to be *ca.* 210 ± 90 \$/kWh$_{\text{e}}$ by 2030 [23]. Taking a PEM electrolysis electricity requirement of 52.5 kWh$_{\text{e}}$/kg$_{\text{H}_2}$, coupled with an estimated compression duty of approximately 0.51 kWh$_{\text{e}}$/kg$_{\text{H}_2}$ up to an operating reactor pressure of 75 bar (from an assumed PEM operating pressure of 20 bar), the total electrical energy input required is 53.0 kWh$_{\text{e}}$ to supply 1 kg of H$_2$ reactant. Hence, if the electricity were stored on batteries for later use in producing H$_2$, the associated capital cost would be *ca.* 11,000 \$/kg$_{\text{H}_2}$ (53 × 210); whereas, the capital cost of compressed hydrogen storage has been estimated as *ca.* 560 ± 30 \$/kg$_{\text{H}_2}$ [24] for large-scale storage. Similarly, performing LT-DAC consumes approximately 1.65 kWh$_{\text{e}}$/kg$_{\text{CO}_2}$, followed by a compression duty of 0.75 kWh$_{\text{e}}$/kg$_{\text{CO}_2}$ to an operating pressure of 75 bar. Hence, the capital cost of storing sufficient reserve electricity on batteries would be *ca.* 130 \$/kg$_{\text{CO}_2}$ (53 × 2.4). The capital cost of compressed CO$_2$ tanks are around 5.5 ± 1.5 \$/kg$_{\text{CO}_2}$ [25].

Hence, the direct use of excess electricity for producing reserve H$_2$ and CO$_2$ leads to lower capital expenditure than using battery storage of electricity to power LT-DAC and PEM electrolysis instead. The above analysis does not

include the capital cost of compressors for raising the H_2 and CO_2 up to storage pressures of 350 and 150 bar, respectively. However, the plant costing analysis (described in **Sec. 11.3**) finds compressor costs of *ca.* \$0.5 $\pm$ 0.1 million for storage of approximately 100 tonnes of H_2 (approximately 5 \$/kg$_{H_2}$), and so the inclusion of compressor costs does not change the conclusion outlined above.

6 Operation of a single large reactor with reserve storage

The storage requirement to operate a single large reactor was modelled according to a similar approach as outlined in **Sec. 3**. The days of storage, and periods of filling storage, were determined as summarised in **Tab. 6**. When using storage, we assumed that storage was consumed to ensure operation at 100% throughput (*i.e.* $n_{i,j,k} = 1$). The plant capacity factor, $\overline{CF}_{\text{plant}; j,k}$, was therefore 100%.

Table 6: The algorithm used to estimate the daily number of operational reactors when operating a single large reactor.

A.	$CF_{i,j,k} \geq \overline{CF}_{j,k}$	$\rightarrow n_{i,j,k} = 1$	Operate at full capacity and fill storage
B.	$\overline{CF}_{j,k} > CF_{i,j,k}$	$\rightarrow n_{i,j,k} = 1$	Operate reactor using stored reserves

Hence, DAC-PtM required the use of reserve storage on 179 $\pm$ 4 days if reliant on offshore wind (averaging across all 30 offshore sites), rising to 188 $\pm$ 6 days for onshore wind (averaging across the 30 in-land sites) – similar to operation under Strategy 2 ("maximise production"), the onshore sites required storage more often than offshore. However, the extent to which the DAC-PtM draws upon storage varies significantly for the case of single, large reactor. For example, only a small quantity of stored reserves need be consumed on a day when $CF_{i,j,k} = 0.9\overline{CF}_{j,k}$; whereas, a very large withdrawal from storage is necessary to operate at full throughput when $CF_{i,j,k} = 0.1\overline{CF}_{j,k}$. Hence, the actual reserve storage capacity, $R_{j,k}$, quantified in terms of effective days at full throughput, was calculated according to **Eq. 8**.

$$R_{j,k} = \sum_{i=1}^{365} 1 - \frac{CF_{i,j,k}}{\overline{CF}_{j,k}} \, , \tag{8}$$

where all terms are as previously defined. For offshore sites, the required storage capacity, averaging across the 30 sites, was equivalent to 88 $\pm$ 3 days, rising slightly to 90 $\pm$ 5 days for the onshore sites.

7 Intermittent operation of a single large reactor without reserve storage

An alternative option if using a single, large reactor is to operate the DAC-PtM intermittently – *i.e.* cease production when insufficient electricity is available. In modelling the intermittent operation of a single reactor, we assumed a 20% operational tolerance, such that the reactor could continue operate down to 80% of full throughput. Hence, the number of operational days was determined, for each site, as summarised in **Tab. 7**.

Table 7: The algorithm used to estimate the daily number of operational reactors when operating a single large reactor intermittently.

A.	$CF_{i,j,k} \geq \overline{CF}_{j,k}$	$\rightarrow n_{i,j,k} = 1$	Operate at full capacity
B.	$\overline{CF}_{j,k} > CF_{i,j,k} \geq 0.8\overline{CF}_{j,k}$	$\rightarrow n_{i,j,k} = CF_{i,j,k}/\overline{CF}_{j,k}$	Operate reactor at reduced capacity
C.	$0.8\overline{CF}_{j,k} > CF_{i,j,k}$	$\rightarrow n_{i,j,k} = 0$	Cease production

The plant capacity factor, $\overline{CF}_{\text{plant } j,k}$, was then calculated according to **Eq. 9**.

$$\overline{CF}_{\text{plant } j,k} = \frac{\sum_{i=1}^{365} n_{i,j,k}}{365} \ .\tag{9}$$

Averaging across the 30 offshore sites gave a typical plant capacity factor of $53 \pm 6\%$, falling to $47 \pm 4\%$ for the onshore sites. Hence, the plant capacity factor is greatly reduced by operating DAC-PtM intermittently with a single large reactor and no reserve storage.

8 Validation of the required storage capacity

To validate the sizing of reserve storage, the fill-level of reserves was modelled across the year for each location. For simplicity, the storage level was considered solely on an energy basis, such that consumption of reserve CO_2 and H_2 was treated using the equivalent energy required to produce them (*i.e.* from electrolysis or DAC, and compression). In addition, the electrical power consumption still required (for compressors and the electric reboiler – see **Sec. 11.1**) was included, accounting for the electricity available from the turboexpanders. Given the treatment of all storage on an energy basis, the depletion of storage therefore corresponds to an effective power withdrawal, $P_{\text{depletion}}$, which was calculated using **Eq. 10**.

$$P_{\text{depletion}} = \dot{m}_{CO_2}(E_{\text{DAC}} + W_{\text{comp. } CO_2}) + \dot{m}_{H_2}(E_{\text{PEM}} + W_{\text{comp. } H_2}) \,,\tag{10}$$

where $\dot{m}_{CO_2}$ and $\dot{m}_{H_2}$ are the mass flowrates (in tonnes per hour) for the withdrawal of CO_2 and H_2, respectively, from storage; E_{DAC} is the overall energy requirement for LT-DAC (in MWh/t_{CO_2}); E_{PEM} is the electricity requirement for PEM electrolysis (in MWh/t_{H_2}); $W_{comp.\ CO_2}$ and $W_{comp.\ H_2}$ are the energy requirements of compressing CO_2 and H_2 up to their respective storage pressures (in MWh/t_{CO_2} and MWh/t_{H_2}, respectively).

Through evaluating **Eq. 10**, and considering the times for which the DAC-PtM required the use of storage against the times during which energy was available to fill the storage, the level of stored reserves was tracked at monthly intervals across the year at each site, under operation Strategies 1 ("minimise storage) and 2 ("maximise production). The size of reserve storage at each location, $R_{j,k}$, was determined by considering the maximum number of times a plant relied on storage within a two-month period.

8.1 Strategy 1

The mass flowrates of CO_2 and H_2 when operating from storage were taken as one quarter of their values when operating the plant at full capacity, given that storage was required to operate one out of the four reactors during low wind availability. We took the one quarter here as indicative of the maximum potential withdrawal flow from storage – *i.e.* during no wind power availability to power one of the four reactors – to ensure a conservative estimate in appraising the size of the storage.

Calculation of the duties for DAC, electrolysis, and compression up to storage pressures found that $P_{depletion}$ is *ca.* 1/4 of the value for the power demand of PtM at full capacity, P_{PtM} – an unsurprising result given that the withdrawal flowrates are one quarter of those at maximum throughput, and considering the dominance of electrolysis, DAC, and compression within the plant power demand. The statement in **Eq. 11** was therefore made, using the result in **Eq. 3** to relate P_{PtM} and $P_{nameplate}$.

$$P_{depletion} \approx \frac{P_{PtM}}{4} = \frac{P_{nameplate}\ \overline{CF}_{j,k}}{4} \ , \tag{11}$$

To track the available stored reserves from month-to-month, we considered the balance between filling of reserves (using available electricity as outlined in **Eq. 6**) and the depletion of stored reserves (by consumption of reserve CO_2, H_2 and electricity). In the mth month ($m = 1$ to 12), and at the jth location during the kth year, the reserves are used for some number of days, $r_{j,k,m}$, causing a depletion, in terms of energy (in MWh), of $24 \times r_{j,k,m} \times P_{depletion}$. The monthly depletion, $D_{j,k,m}$, can then be expressed as a fraction of annual electricity generation (MWh/MWh) by dividing through as shown in **Eq. 12**.

$$D_{j,k,m} = \frac{24 \times r_{j,k,m} \times P_{depletion}}{24 \times 365 \times \overline{CF}_{j,k} P_{nameplate}} = \frac{r_{j,k,m}\ P_{depletion}}{365 \times \overline{CF}_{j,k}\ P_{nameplate}} \ , \tag{12}$$

where all terms are as previously defined. Substituting **Eq. 11** in to **Eq. 12** then yields the simplified result in **Eq. 13**.

$$D_{j,k,m} \approx \frac{r_{j,k,m}}{4 \times 365} \; . \tag{13}$$

The value of $D_{j,k,m}$ was determined by using the output of the algorithm in **Tab. 3** to find $r_{j,k,m}$ – the number of days reliant upon reserves (scenario E) each month.

Over the same month, the energy available to replenish the storage (as a fraction of annual generation) was given by truncating the summation in **Eq. 6** across a given month (*e.g.* from $i = 32$ to $i = 59$ for February), denoted as $E_{j,k,m}$. Consequently, the storage level at the end of a month was given by **Eq. 16**.

$$L_{j,k,m} = L_{j,k,m-1} + E_{j,k,m} - D_{j,k,m} \; , \tag{14}$$

where $L_{j,k,m}$ denotes the level at the end of the month (m) and $L_{j,k,m-1}$ is the level at the end of the previous month ($m - 1$). Using **Eq. 16** allows tracking of the level of stored reserves across a year at each site, for some specified capacity. For each location, the capacity of reserve storage, $R_{j,k}$, was selected as the maximum number of days in a two-month period for which the plant required reserve storage, which typically varied between 10 and 30 days for the various locations. For ease of comparison between different sites with varying capacities, the storage level was then normalised against the maximum fill level. The maximum fill level, $L_{j,k}^{\max}$, was given by **Eq. 15**, the derivation of which followed the same logic as **Eq. 13**, considering filling storage to enable $R_{j,k}$ continuous days of operation.

$$L_{j,k}^{\max} = \frac{s_{j,k} \times P_{\text{depletion}}}{365 \times \overline{CF}_{j,k} P_{\text{nameplate}}} \approx \frac{s_{j,k}}{4 \times 365} \; . \tag{15}$$

Therefore, the relative storage fill level at the end of each month was given by $L_{j,k,m}/L_{j,k}^{\max}$, yielding the results shown in **Fig. 4**.

8.2 Strategy 2

When operating under Strategy 2, the maximum potential withdrawal flow from storage was taken as equivalent to that required to run a single reactor – one quarter of the maximum flow. Therefore, the depletion power, $P_{\text{depletion}}$, was the same as that given by **Eq. 11** for Strategy 1, and the monthly depletion was as given by **Eq. 13**. The energy available for filling the storage in a given month, $F_{j,k,m}$ was given by truncating the summation in **Eq. 7** over a given month, as previously described. Hence, the fill-level at the end of a given month was given by

$$L_{j,k,m} = L_{j,k,m-1} + F_{j,k,m} - D_{j,k,m} \; , \tag{16}$$

where all terms are as previously defined. The relative storage level was then determined by normalising against the maximum fill capacity, $L_{j,k}^{\max}$, calculated according to **Eq. 15**. The resulting trajectories of storage levels are summarised in **Fig. 5** for Strategy 2.

9 Storage levels when using a single large reactor

The same approach as outlined in **Sec. 8** was used to track the storage levels across a year when operating one large PtM reactor, with the storage capacities days found previously in **Sec. 6** (*ca.* 90 days on average). The results, shown in **Fig. 4** for exemplar onshore and offshore locations, confirm the storage size as appropriate. The sites, mostly, do not empty their stored reserves, and none generate an excessive surplus. Furthermore, the storage levels show good circularity across the year, beginning and ending the year roughly half-full. The storage levels are expressed as a relative storage level (normalised against the maximum fill capacity) to account for changes to the required storage sizes between the locations.
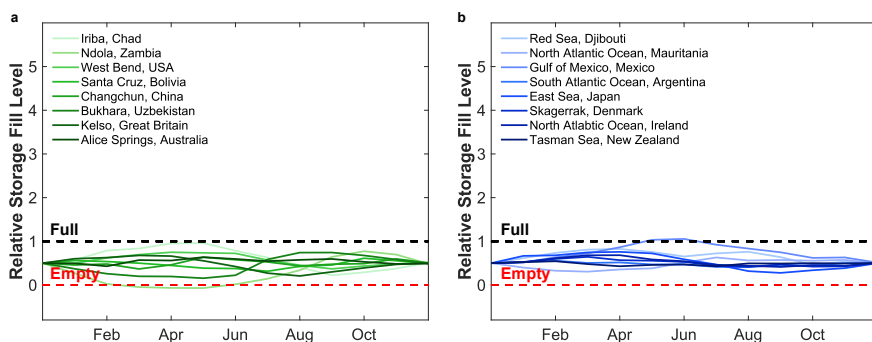

Fig. 4: The level of stored reserves across a year when operating DAC-PtM with one large reactor, reliant upon **a** onshore wind power in 2017, or **b** offshore wind power in 2019.

10 Using different numbers of reactors

The analysis in **Sec. 3** was extended to consider alternative numbers of reactors. The plant capacity factors and required storage capacities are shown in **Fig. 5** as a function of the number of parallel reactors under Strategy 1 ("minimise storage") and Strategy 2 ("maximise production"). The required storage capacity is expressed in number of days equivalent for running one of the four parallel reactors – *i.e.* running 1 out of 2 reactors for a day requires double the amount reactants as running 1 out of 4 reactors (for the same overall plant scale), and so 1 day of storage for a 2 reactor plant is actually equivalent to 2 days storage on the basis of a 4-reactor plant layout *et cetera*.

Under Strategy 1 ("minimise storage"), the plant capacity factor does not change substantially with changes to the number of reactors, decreasing by only 2%. For Strategy 2 ("maximise storage"), in which storage is used to boost the
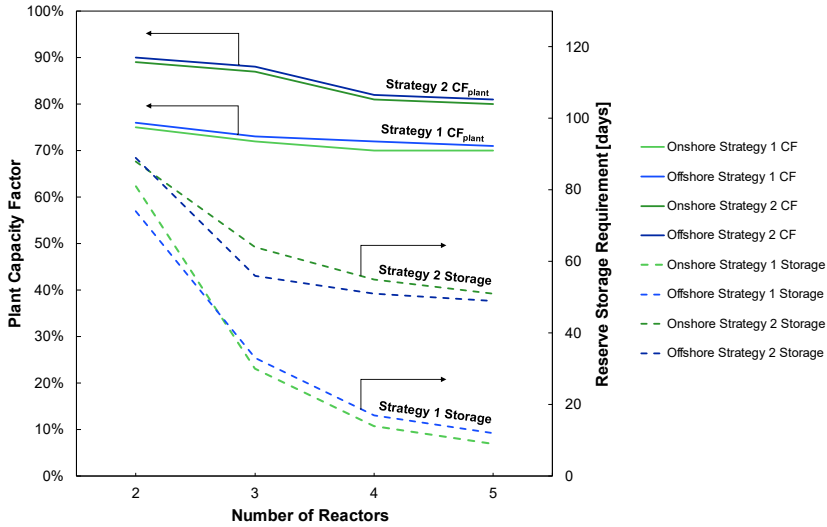
Fig. 5: The plant capacity factor (solid lines, left axis) and required reserve storage capacity (hatched lines, right axis) for the onshore and offshore wind farm sites, plotted as a function of the number of reactors for methanol synthesis, which spans 2 to 5. The plotted values are an average across the thirty onshore and offshore sites.

number of operational reactors, increasing the number of reactors does have a more sizeable effect on the plant capacity factor, which decreases by around 6% when changing between 2 and 5 reactors. The storage requirement falls sharply when increasing from 2 to 3 reactors; the storage required continues to fall as the number of reactors increases beyond two, albeit with diminishing returns as the number of reactors reaches 5. The use of 4 reactors therefore represents a sensible choice for DAC-PtM, with storage reduced *versus* using fewer reactors, and without adversely compromising plant capacity factor.

11 Process modelling

11.1 Detailed process description

The process flow diagram for methanol production *via* DAC-PtM is shown in **Fig. 6**. The CO_2 needed for DAC-PtM is taken from an air feed (stream 1 in **Fig. 6**) *via* low-temperature direct air capture (LT-DAC), and green H_2 is produced by polymer electrolyte membrane (PEM) electrolysis of water (stream 2) – a process which also generates an oxygen by-product (stream 3). The water supplied to the electrolysis comes from a reverse osmosis (RO) facility, although the modelling also considers an optimistic scenario in which fresh water is available for direct supply to the electrolysis. The DAC requires electrical energy, primarily for the fan assemblies to drive air through the adsorbent capture units, and a heat duty for the subsequent desorption and
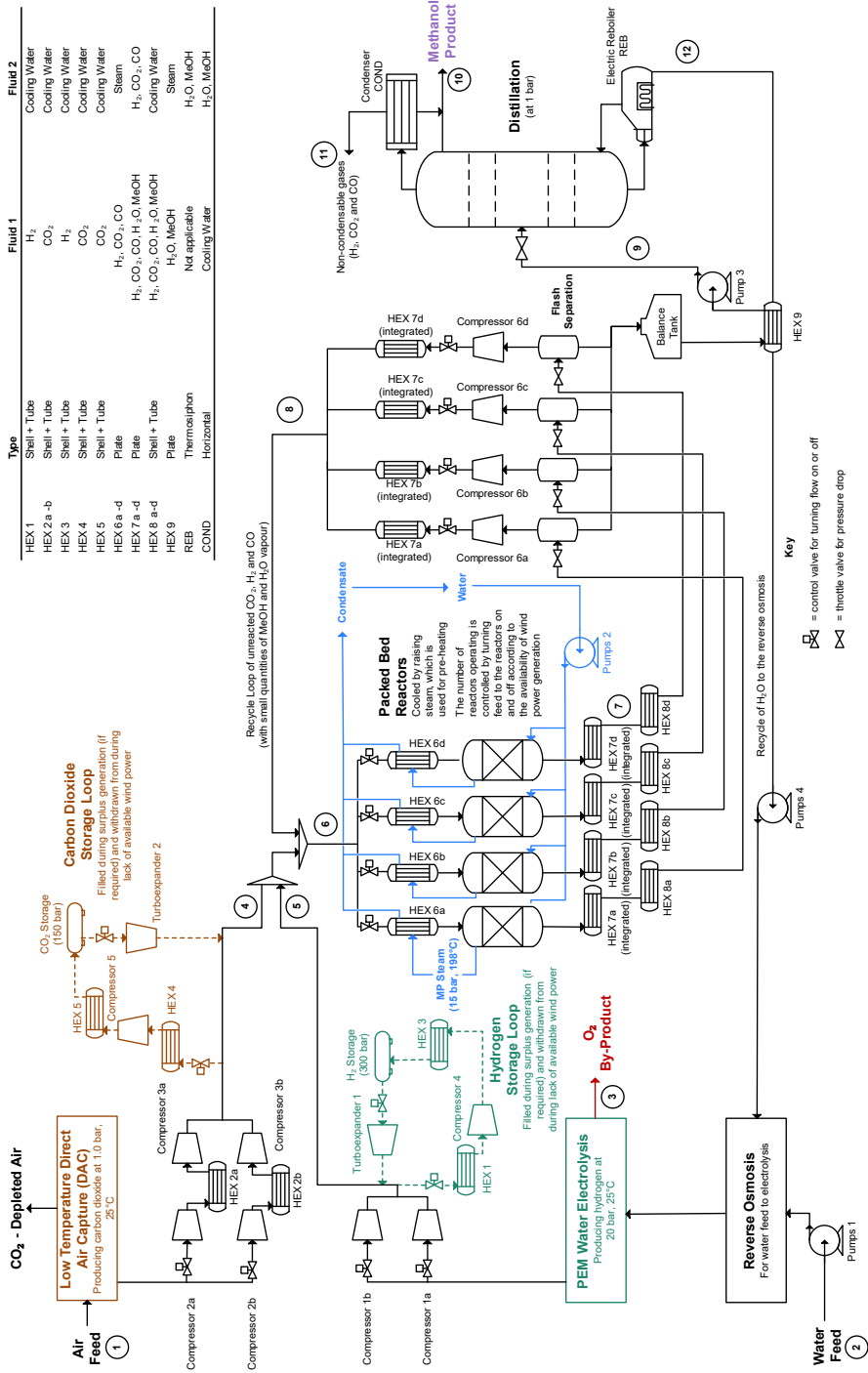
Fig. 6: Process flow diagram for the production of MeOH from CO_2, captured from air, using H_2 produced by electrolysis. The storage loops for CO_2 and H_2 are indicated in orange and green, respectively. The CO_2 and H_2 are fed to the reactors for methanol synthesis. A flash separation removes the majority of H_2O and MeOH in the reactor outlet, leaving a gas mixture of predominantly CO, CO_2, and H_2, followed by distillation to separate high-purity MeOH from the water. The abbreviation HEX refers to a heat exchanger.

elution of adsorbed CO_2. The DAC produces CO_2 at 1 bar, which passes through multi-stage compression with inter-cooling by water.

A wind farm, either onshore or offshore, is the source of renewable electricity for the entire plant. Storage of CO_2, H_2, and electricity enables continuous operation of downstream methanol production despite the intermittent electricity supply.

When operating fewer out of the four reactors for DAC-PtM, the CO_2 and H_2 storage tanks are filled using any extra electricity available. The storage loop for CO_2, shown in orange in **Fig. 6**, compresses the CO_2 up to 150 bar, with subsequent cooling down to 298 K with cooling water. The storage loop for H_2, highlighted in green in **Fig. 6**, stores H_2 at 300 bar, owing to the lower density of H_2 than CO_2, again with cooling down to 298 K after compression using cooling water. During very low wind power availability (described in **Sec. 3**), the CO_2 and H_2 are withdrawn from storage, passing through a turboexpander to recover energy and bring the streams back down to the reactor operating pressure (*ca.* 50 to 100 bar). The process pressure varies between the considered optimism scenarios; the optimistic case reactor pressure is 50 bar, the base case uses 75 bar, and the pessimistic case uses 100 bar. Reducing the reactor pressure allows for greater energy recovery by the turboexpanders.

The feed streams of CO_2 and H_2 (streams 4 and 5, respectively, in **Fig. 6**) are mixed, combined with a recycle, and delivered to the operational reactor(s). The feed to the reactor (stream 6) contains a slight excess of H_2 to improve selectivity towards methanol, albeit at the expense of a larger recycle flowrate. A typical ratio of $H_2/CO_2 = 4$ is used [26].

The exothermic formation of methanol evolves heat within the reactor(s), which is removed by the raising of medium-pressure steam to effect temperature control of the reactor(s). The steam is used to pre-heat the feed gas (stream 6) up to the reactor entry temperature of 523 K. The feed preheating and reactor cooling are directly integrated in some industrial reactor designs [27, 28]. However, the dynamic operation of reactors (*i.e.* regularly bringing reactors on- and off-line) is better suited to a water-cooled reactor design, given that the safe temperature control of a reactor is not directly dependent on the time-variant flow of feed gas.

The two overall reactions in each reactor are the formation of methanol (**R17**), and the production of carbon monoxide *via* the reverse water gas shift reaction (**R18**).

$$CO_2 + 3H_2 \rightleftharpoons CH_3OH + H_2O \, , \tag{17}$$

$$CO_2 + H_2 \rightleftharpoons CO + H_2O \, , \tag{18}$$
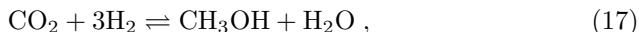
Therefore, the outlet gas from the reactor (stream 7) contains unreacted CO_2 and H_2, as well as MeOH, H_2O, and CO produced in the reactor. The MeOH and H_2O are predominantly separated from the outlet gas by flash separation at 298 K and 5 bar below the methanol synthesis pressure (leaving as stream 9), resulting in a gas stream of mostly CO, CO_2, and H_2 (stream 8) for

recycle to the reactor. The recycled CO also participates in the production of methanol *via* the reverse of **R18** followed by **R17**, and so does not accumulate in the system. The recycle stream is compressed back up to the process pressure and heated to the reactor feed temperature, largely achieved by heat-integration with the cooling of the reactor outlet (heat exchanger network HEX 7a to d in **Fig. 6**). Cooling water performs the remainder of the cooling duty to bring the reactor outlet (stream 7) down to the flash temperature of 298 K.

The mixture of H_2O and MeOH leaving the flash (stream 9) passes to a distillation step, operating near atmospheric pressure, to separate high-purity (99.9 mol%) methanol (stream 10). The feed to the distillation, arriving from the flash, also contains a trace quantity of dissolved gas (mostly CO_2), which is vented at the condenser (stream 11) to avoid accumulation. The water leaving from the electric reboiler (stream 12), performs the pre-heating of the feed to the distillation column, before being recycled to the water electrolysis stage. The water recycle accounts for *ca.* 2/3 of the total water demand of the electrolysis.

11.2 Full overview of model assumptions and features

The process calculations are undertaken using the following assumptions and modelling features:

- The operating and capital expenditure of onshore and offshore wind farms are estimated using literature values. The offshore wind farm capital cost values include the cost of connecting the offshore site to the PtM facility on the mainland; for the onshore case, we assume the wind farm and PtM facility are co-located.
- The electrical demand is assumed as the dominant source of operating expenditure for reverse osmosis. The cost of acquiring access to water (*e.g.* brackish water) is not considered.
- The capital cost of providing cooling water is not considered. Instead, the cost of providing cooling water is estimated using standard correlations for the cost of cooling water utility [29].
- The electrical and heating duties of DAC and electrolysis are estimated using literature values.
- The DAC and electrolysis are assumed to produce pure CO_2 and H_2, respectively.
- The potential for H_2 slip (*i.e.* slow escape loss of H_2) from storage is neglected in considering the required storage capacity.
- The perfect mixing of gases is assumed throughout.
- The compression and expansion duties of CO_2 and the recycle stream are estimated assuming the ideal-gas law, modulated using an isentropic efficiency, η, to account for irreversible losses. The work, W, of compression or expansion between pressures p_1 and p_2

is given by **Eq. 19**.

$$W = \frac{1}{\eta} \frac{\gamma - 1}{\gamma} R T_1 \left[\left(\frac{p_2}{p_1} \right)^{1 - \frac{1}{\gamma}} - 1 \right] , \qquad (19)$$

where γ is the heat capacity ratio, T_1 is the initial temperature, and R is the molar gas constant. The values of γ are calculated using correlations provided by NIST [30].

- The compression of H_2 and its expansion back down to reactor operating pressures is modelled using the Redlich-Soave-Kwong (RSK) equation of state for H_2 [31]. An isentropic efficiency is again used to account for irreversible losses.

- The reactor model uses typical values for the outlet conversion of CO_2, but we apply the established Vanden Bussche and Froment kinetic model [32], for copper-zinc oxide catalysts, to estimate the selectivity towards methanol at a given outlet conversion as a function of reactor operating pressure, temperature, and feed composition (including the recycled CO in addition to CO_2 and H_2). The kinetic model is integrated with respect to conversion, assuming an isothermal temperarature profile and neglecting radial concentration profile effects. The neglection of radial concentration effects is acceptable for the reactor type considered in the model here, which consists of many small packed bed reactor tubes through which the reactant gas flows, with steam raised from water in the surrounding shell. Isothermal reactor designs for methanol synthesis are also widely used industrially [27]. The yield achieved by the industrial catalyst is estimated using a spread of reported values.

- The Rachford-Rice equation is used to model the flash separation of water and methanol from the reactor outlet gas. Any dissolved gases in the crude MeOH and H_2O product are assumed to have negligible influence upon the vapour-liquid equilibrium (VLE) of MeOH and H_2O. Therefore, a binary two-constant Margules activity coefficient model is used for the VLE of methanol and water [33], coupled with Antoine parameters. The dissolution of CO, CO_2, and H_2 into the liquid leaving the flash is modelled using Henry's law constants.

- The distillation model also assumes binary VLE behaviour of methanol and water within short-cut methods: Fenske's equation for the minimum reflux ratio, R_m, and Underwood's equations for the minimum number of stages. The actual number of stages is estimated using the Gilliland correlation, and a reflux ratio of $1.4R_m$ is assumed as sufficient. Any dissolved CO, CO_2, and H_2 leaves *via* the gas outlet at the condenser and does not accumulate.

- All heat exchangers are modelled using assumed heat transfer coefficients for the following process-service fluid configurations: gas-gas

(30 W m^{-2} K^{-1}), water-gas (200 W m^{-2} K^{-1}), refrigerant-gas (250 W m^{-2} K^{-1}), steam-liquid (1000 W m^{-2} K^{-1}), steam-gas (300 W m^{-2} K^{-1}) [34]. Losses are neglected when modelling the heat-integration.

- The cost of land purchase is not considered.
- Assumed installation factors are taken from the literature for the process equipment [34].

11.3 Determination of the operating and capital expenditures

The cost of methanol production *via* DAC-PtM is considered through the operating expenditure (OPEX) of daily DAC-PtM operation, and the capital expenditure (CAPEX) of erecting the facility. To investigate the potential range of production costs, and the scope for cost reduction with technology improvements, the process is investigated under three different optimism scenarios: base, optimistic, and pessimistic.

The values used in the process calculations and OPEX determinations are listed in **Tab. 8** below, including the different OPEX values for onshore and offshore wind farms. Using the values tabulated in **Tab. 8**, the entire operating expenditure for the PtM process is calculated. For example, the contribution of PEM electrolysis is given by **Eq. 20**

$$
\begin{aligned}
\text{OPEX}_{\text{PEM}}[\$/\text{kg}_{\text{MeOH}}] = {} & \frac{\dot{m}_{\text{H}_2}[\text{kg}_{\text{H}_2}\text{hr}^{-1}]}{\dot{m}_{\text{MeOH}}[\text{kg}_{\text{MeOH}}\text{hr}^{-1}]} \times E_{\text{PEM}}[\text{MWh}_{\text{e}}\ \text{kg}_{\text{H}_2}^{-1}] \\
& \times \text{OPEX}_{\text{wind}}[\$\ \text{MWh}_{\text{e}}^{-1}],
\end{aligned} \tag{20}
$$

where the value of E_{PEM} is taken from **Tab. 8**, and the required flowrate of fresh H_2 to be produced by electrolysis, $\dot{m}_{\text{H}_2}$, is calculated from the reactor model (*i.e.* the conversion and selectivity values in **Tab. 8**). Likewise, the OPEX contribution of the compressors is calculated according to

$$
\begin{aligned}
\text{OPEX}_{\text{comp}} = {} & \left(\sum_{n=1}^{6} W_n^{\text{comp}}\ [\text{kWh}_{\text{e}}\text{kg}_{\text{MeOH}}^{-1}] - \sum_{m=1}^{2} W_m^{\text{turbo}}\ [\text{kWh}_{\text{e}}\text{kg}_{\text{MeOH}}^{-1}] \right) \\
& \times \text{OPEX}_{\text{wind}}[\$\ \text{kWh}_{\text{e}}^{-1}],
\end{aligned} \tag{21}
$$

where W_n^{comp} is the energy duty of the nth compressor assembly (as shown in **Fig. 6** running $n = 1$ to 6), which has energy recovery from the turboexpanders subtracted (W_m^{turb}, where $m = 1$ to 2) – noting that the number of operating compressors and turboexpanders changes depending upon the operating configuration of the plant (*i.e.* whether or not the storage tanks are being filled or emptied). Similar calculations yield the OPEX contribution from LT-DAC, cooling water duties, and the provision of water to the electrolysis by

RO; however, the optimistic case assumes that fresh water is available without the need for RO. Another consideration in the calculation of OPEX is the replacement of spent catalyst. The deterioration of current copper-zinc oxide catalysts is a known issue when synthesising methanol from CO_2 and H_2, likely due to the accumulation of adsorbed water and the subsequent promotion of sintering [35]. The base and pessimistic cases use currently reported values for catalyst lifetime and cost, whereas the optimistic case assumes improved longevity according to reported catalyst developments [36].

Table 8: The values we use in process calculations and the determination of operating expenditure (OPEX) to produce methanol from CO_2 under three modelled scenarios.

Parameter	Base	Optimistic	Pessimistic	Ref.
Onshore wind farm OPEX [$ MWh$_e^{-1}$]	3.5 ± 2	1.5 ± 0.5	7 ± 4	[37, 38]
Offshore wind farm OPEX [$ MWh$_e^{-1}$]	22 ± 5	5 ± 2	31 ± 5	[39–41]
PEM electrical req., E_{PEM} [kWh$_e$ kg$_{H_2}^{-1}$]	52.5 ± 2.5	43.8 ± 2.0	62.7 ± 2.5	[36, 42]
RO energy req., E_{RO} [kWh$_e$ m$_{H_2O}^{-3}$]	3.0	-	4.5	[43]
DAC electrical req., E_{DAC} [kWh$_e$ kg$_{CO_2}^{-1}$]	0.25 ± 0.07	0.15 ± 0.02	0.40 ± 0.05	[44, 45]
DAC heat req., H_{PEM} [kWh$_{th}$ kg$_{CO_2}^{-1}$]	1.4 ± 0.25	1.0 ± 0.20	2.0 ± 0.35	[44, 45]
Cooling water OPEX [$ m$_{H_2O}^{-3}$]	0.30	0.20	0.70	[29]
Isentropic efficiency, η	85%	90%	70%	[46]
Reactor pressure [bar]	75	50	100	[36]
CO_2 conversion, X	$15 \pm 2\%$	$40 \pm 5\%$	$10 \pm 1\%$	[26]
MeOH selectivity, S [a]	$65 \pm 3\%$	$99 \pm 0.5\%$	$60 \pm 5\%$	[32, 47][a]
MeOH Yield, Y[mol$_{MeOH}$ kg$_{cat}^{-1}$ h^{-1}]	16 ± 3	40 ± 5	8 ± 1	[47]
Catalyst cost [$ kg$_{cat}^{-1}$]	10 ± 3	12 ± 5	16 ± 8	[48]
Catalyst lifetimes [years]	2	5	0.5	[36]
Maintenance [% CAPEX p.a.][b]	2%	1%	2%	[34]

[a] selectivity values for the base and pessimistic cases are estimated using the kinetic model [32], whereas the optimistic case value represents a potential state-of-the-art catalyst [47].
[b] excluding the wind farm CAPEX, as wind farm maintenance is already included in the OPEX values for electricity generation.

Given the use of multiple reactors, to be taken on- and off-line according to wind power availability, the flowrates vary across the plant according to the number of active reactors. Therefore, the required operating expenditure for methanol production also differs according to the number of active reactors, due to changes in the required duties for LT-DAC, electrolysis, compressors, and heat exchangers, as a function of plant throughput. A time-averaged value for the plant operating expenditure, $\overline{\text{OPEX}}$, is therefore calculated using **Eq. 22**.

$$\overline{\text{OPEX}} = \frac{n_{sto}\text{OPEX}_{sto} + \sum_{i=1}^{4} n_i\text{OPEX}_i}{365} \,, \tag{22}$$

where n_{sto} is the number of days spent reliant upon storage; OPEX_{sto} is the plant OPEX when using H_2 and CO_2 from the reserve storage; n_i is the number of days with i active reactors (excluding days when using storage for $i = 1$); and OPEX_i is the total operating expenditure with i active reactors.

The capital expenditure (CAPEX) of the plant is also estimated under the same three cases (base, optimistic, and pessimistic); pertinent assumptions and

values are listed in **Tab. 9**. The costs of compressors, heat exchange equipment, and separation vessels are calculated in 2010 US Dollars, and corrected to a 2019 basis with Chemical Engineering Plant Cost Indices (CEPCI) of 532.9 and 607.5 for 2010 and 2019, respectively [49, 50]. The cost of the packed bed reactor for methanol synthesis is estimated by scaling a base cost provided by [51] according to the mass of catalyst required, yielding a cost in 2006 US Dollars which is corrected to 2019 with a CEPCI of 499.6 for 2006 [52].

Table 9: All values we use in the determination of capital expenditure (CAPEX) under each optimism case .

Parameter	Base	Optimistic	Pessimistic	Ref.
Onshore wind farm [$ kW$_e^{-1}$]	$1,100 \pm 250$	800 ± 100	$2,100 \pm 400$	[38, 53]
Offshore wind farm [$ kW$_e^{-1}$]	$2,500 \pm 500$	$1,700 \pm 200$	$4,200 \pm 500$	[53, 54]
Offshore wind farm export distance [km]	20	5	50	[55]
Installation of offshore export cable [$/m]	150 ± 20	65 ± 10	660 ± 120	[54]
PEM system [$ kW$_e^{-1}$]	600 ± 200	360 ± 40	$1,500 \pm 400$	[36, 56]
PEM stack replacement [% initial CAPEX]	20%	5%	40%	[57]
PEM stack lifetimes [years]	6	15	2	[28]
LT-DAC system [$ tn$_{CO_2}^{-1}$ p.a.]	800 ± 150	450 ± 100	1300 ± 250	[44]
H$_2$ storage tank [$ kg$_{H_2}^{-1}$]	560 ± 30	400 ± 70	730 ± 150	[24, 58]
CO$_2$ storage tank [$ kg$_{CO_2}^{-1}$]	18 ± 3	14 ± 2	26 ± 4	[25]
Battery storage [$ kWh$_e^{-1}$]	210 ± 90	130 ± 40	250 ± 100	[23]
RO capital [$ m$_{H_2O}^{-3}$ per day]	1,900	-	2,200	[59]
MeOH reactor [$_{2006}$]	$\text{Cost} = 20,100(\text{Catalyst Mass [kg]})^{0.6} \pm 15\%$			[51]
Compressor [$_{2010}$]	$\text{Cost} = 260,000 + 2,700(\text{Duty [kW]})^{0.75} \pm 10\%$			[34]
Heat exchanger [$_{2010}$]	$\text{Cost} = 28,000 + 54(\text{Area [m}^2])^{1.2} \pm 15\%$			[34]
Reboiler [$_{2010}$]	$\text{Cost} = 28,000 + 54(\text{Area [m}^2])^{0.9} \pm 10\%$			[34]
Pressure vessel [$_{2010}$]	$\text{Cost} = 17,400 + 79(\text{Shell Mass [kg]})^{0.85} \pm 5\%$			[34]
Distillation tray [$_{2010}$]	$\text{Cost} = 340 + 640(\text{Area [m}^2])^{1.9} \pm 5\%$			[34]

12 Economic calculations

The methanol selling price is determined *via* a net present value (NPV), using the weighted average cost of capital (WACC) as the discount rate as shown in **Eq. 23**.

$$\text{NPV} = -\text{CAPEX} + \sum_{i=1}^{15} \frac{\text{Net Cash Flow}_i}{(1 + \text{WACC})^i} , \tag{23}$$

where i refers to the ith year of plant operation, up to the economic plant lifetime of 15 years. The WACC rates used are 5%, 4%, and 7% for the base, optimistic, and pessimistic cases, respectively.

The incoming revenue streams for the sale of methanol, oxygen, and surplus electricity are calculated as follows:

$$\text{MeOH revenue [\$]} = \overline{CF}_\text{plant} \times \text{Annual plant capacity (50,000 t}_\text{MeOH}) \\ \times \text{MeOH price [\$/t}_\text{MeOH]} , \tag{24}$$

$$\text{O}_2 \text{ revenue } [\$] = \overline{CF}_{\text{plant}} \times \text{ Annual plant capacity } (50{,}000 \text{ t}_{\text{MeOH}})$$
$$\times \text{ O}_2 \text{ per unit MeOH } \times \text{ O}_2 \text{ price } [\$/\text{t}_{\text{MeOH}}] \,, \tag{25}$$

$$\text{Elec. revenue } [\$] = CF \times \text{ Wind farm size } [\text{MW}] \times \text{ Operational hours } (8{,}000)$$
$$\times \text{ Annual surplus } [\text{MWh}_{\text{surp}}/\text{MWh}_{\text{gen}}]$$
$$\times \text{ Fraction of surplus sold}$$
$$\times \text{ Electricity sale price } [\$/\text{MWh}] \,, \tag{26}$$

where $\overline{CF}_{\text{plant}}$ and CF are as previously defined in **Eqs. 4** and **1**, respectively.

The determination of revenue from selling oxygen (**Eq. 25**) requires quantification of the O_2 by-production per unit MeOH. The process model finds a fresh hydrogen requirement of $0.19 \pm 0.01 \text{ kg}_{\text{H}_2}/\text{kg}_{\text{MeOH}}$ across the three optimism cases; from the stoichiometry of H_2 production from H_2O, the resulting by-production of O_2 is $1.50 \pm 0.08 \text{ kg}_{\text{H}_2}/\text{kg}_{\text{MeOH}}$. Even though O_2 is always by-produced by the DAC-PtM facility, an over-the-fence sale requires a suitable local buyer (*e.g.* an epoxidation process). An oxygen price of \$40 per tonne of O_2 is taken in the base case, and \$55 per tonne of O_2 in the optimistic case [60]; in the pessimistic case we assume no local buyers and hence no oxygen sale. Despite the large volume of O_2 for sale (75,000 tonne/year), the results in **Fig. 12** show the influence of O_2 revenue on methanol selling price as very slight.

For the sale of surplus electricity as a revenue stream (**Eq. 26**), we consider that the surplus electricity is stored in batteries for later sale to the grid at a pre-agreed price. The use of battery storage is motivated by the fact that the periods of electricity surplus (*e.g.* windy days) may not correspond with times at which there is demand from the grid to purchase the surplus electricity. In the base case, electricity is sold at \$50 per MWh, and the optimistic and pessimistic cases sell electricity at \$60 and \$25 per MWh, respectively. Additionally, in the pessimistic case we assume that only 50% of the surplus electricity can be sold due to insufficient demand from the grid (*e.g.* due to strong performance of grid-integrated renewables such as solar). Instead of selling or storing electricity, the surplus can be directed to produce extra H_2 or CO_2 as saleable products. In such an instance, the H_2 and CO_2 revenues are given by **Eqs. 27** and **28**, respectively, in which E_{PEM} and E_{DAC} refer to the electricity demands of PEM electrolysis and LT-DAC respectively, and H_{DAC} is the regenerative heat demand of LT-DAC (which is provided electrically in the absence of waste heat – discussed further in **Sec. 11.1**).

$$\begin{aligned}
H_2 \text{ revenue } [\$] = {} & CF \times \text{Wind farm size [MW]} \times \text{Operational hours (8,000)} \\
& \times \text{Annual surplus } [\text{MWh}_{\text{surp}}/\text{MWh}_{\text{gen}}] \\
& \times \frac{H_2 \text{ price } [\$ \text{ kg}_{H_2}^{-1}]}{E_{\text{PEM}} \ [\text{kWh}_e \ \text{kg}_{H_2}^{-1}]} \ ,
\end{aligned}$$
(27)

$$\begin{aligned}
CO_2 \text{ revenue } [\$] = {} & CF \times \text{Wind farm size [MW]} \times \text{Operational hours (8,000)} \\
& \times \text{Annual surplus } [\text{MWh}_{\text{surp}}/\text{MWh}_{\text{gen}}] \\
& \times \frac{CO_2 \text{ price } [\$ \text{ kg}_{CO_2}^{-1}]}{E_{\text{DAC}} \ [\text{kWh}_e \ \text{kg}_{H_2}^{-1}] + H_{\text{DAC}} \ [\text{kWh}_e \ \text{kg}_{H_2}^{-1}]} \ ,
\end{aligned}$$
(28)

Considering H_2 sale prices in the range \$3 to \$6 per kg of H_2 [61], the resulting selling price of methanol only decreases by *ca.* \$ 200 per tonne of MeOH *versus* the sale of surplus electricity, with approximately 0.1 tonnes of surplus H_2 produced per tonne of MeOH, requiring increased expenditure on hydrogen storage.

The sale of surplus CO_2 for \$40 to 180 per tonne of CO_2 [62] in fact results in an increase in the selling price of methanol by *ca.* \$300 per tonne of MeOH *versus* the sale of surplus electricity, even though approximately 0.6 tonnes of surplus CO_2 is captured per tonne of MeOH product. The result points to the important fact that current carbon pricing means that the price of electricity often exceeds the value of CO_2 captured by DAC, thus, providing further justification for using DAC to produce value-added chemicals, such as methanol, rather than purely utilising DAC for carbon capture and sequestration (*i.e.* DACCS).

13 Breakdown of plant power demand under the base, optimistic, and pessimistic cases

The power demand of DAC-PtM, at full throughput, is summarised in **Tab. 10** for the base, optimistic and pessimistic cases. For the power contribution of DAC, the energy required to heat the sorbent for regeneration (*i.e.* desorption of CO_2) is included, whilst the energy requirement of heating in **Tab. 10** refers to all other heating on the plant – namely the reboiler for the distillation column. Under the base and pessimistic cases, all heating is provided electrically unless integrated with cooling on the plant (**Fig. 6**); whereas, the optimistic case assumes free access to low-grade waste heat for regeneration of the sorbent and the reboiler (both of which require temperatures of only *ca.* 373 K).

Table 10: A breakdown of the power consumption by DAC-PtM, when operating at full throughput, under the base, optimistic, and pessimistic cases.

Process Area	Power demand [MW_e]		
	Base	Optim.	Pessim.
Electrolysis	58.73	48.99	87.67
DAC	13.23	1.20	24.05
CO_2 Compression	5.97	5.06	10.05
Non-CO_2 Compression	1.11	0.45	1.79
Heating	3.17	0.00	3.21
Pumping and Reverse Osmosis	0.03	0.02	0.04

14 Life cycle analysis

In **Tab. 11**, a summary is given of previously reported GWP values from life cycle analyses of methanol production when reliant upon fossil fuels for the generation of syngas. Averaging across the reported LCA studies for which natural gas was the primary feedstock yields an estimated GWP of 780 kg_{CO_2eq}/t_{MeOH}, rising to 3,100 kg_{CO_2eq}/t_{MeOH} when using coal.

Table 11: A summary of previously reported global warming potential (GWP) values from life cycle analyses for methanol production when reliant upon fossil fuels for the generation of the syngas feedstock for the methanol synthesis.

Global warming potential [kg_{CO_2eq}/t_{MeOH}]	Notes on the fossil fuel feedstock to the process	Ref.
915	Steam reforming of natural gas	[63]
735	Steam reforming of natural gas	[64]
730-1,070	Steam and autothermal reforming of natural gas	[65]
462	Steam reforming of natural gas	[66]
764	Reforming of natural gas	[67]
1,644	Coal gasification	[63]
3,474	Coal gasification	[68]
2,970	Coal gasification	[66]
4,400	Coal gasification	[67]

The life cycle inventory of emission factors are summarised in **Tab. 12**. The assumptions regarding the water feed to the electrolysers and catalyst were applied across investigated scenarios, whilst the assumed emissions intensity of the electricity provision were specific to each of the offshore wind power, onshore wind power, and grid scenarios.

The life cycle GWP of onshore wind power has been estimated as ranging from 5.0 to 28.2 kg_{CO_2eq}/MWh_e under varying assumptions around farm location and lifetime [69–72]. An indicative worldwide average of 11.0 kg_{CO_2eq}/MWh_e was applied here. Estimates for offshore wind power range from 7.8 to 44.0 kg_{CO_2eq}/MWh_e [72–76]. Averaging across sources, which

cover varying worldwide locations, yielded 25.0 kg_{CO_2eq}/MWh_e. The GWP-intensity of the European energy mix was collected from the Simapro [76] and Ecoinvent [77] databases. The database estimate for Europe (392 kg_{CO_2eq}/MWh_e) slightly exceeds a previously reported literature estimate of 334 kg_{CO_2eq}/MWh_e [78] for only the EU27 countries – the more conservative of the two estimates was used here. The GWP associated with a Brazilian grid mix was taken as 155 kg_{CO_2eq}/MWh_e from a detailed breakdown of the Brazilian energy mix [79]. A slightly lower emissions intensity of 130 kg_{CO_2eq}/MWh_e has been reported elsewhere [80], albeit with a less transparent methodology. The emission-intensity of the Chinese grid given by Simapro [76] and Ecoinvent [77] (1044 kg_{CO_2eq}/MWh_e) is likely outdated, and drastically exceeds recently reported estimates of 599 kg_{CO_2eq}/MWh_e [81] and 557 kg_{CO_2eq}/MWh_e [82] – an average of the latter two sources was used here.

The breakdowns of GWP emissions determined by LCA are summarised in **Tab. 13** for offshore and onshore wind power scenarios, and in **Tab. 14** for the grid electricity scenarios. The GWP values associated with electrolysis, DAC, compression (of CO_2 and non-CO_2), heating, the pumping and reverse osmosis (RO) are all determined from solely the energy consumption of each operation; the GWP associated with construction of the equipment for each operation (*e.g.* constructing a compressor or electrolyser stack) are not included. The GWP associated with providing the water for electrolysis arises from the softening of the water, with further GWP arising then from the RO processing of the water prior to electrolysis to remove unwanted salts such as sodium chloride. The LCA also accounts for the emission of CO_2 at the condenser during distillation (**Sec. 11.1**).

Table 12: Life cycle inventory (LCI) of emission factors and assumptions for each investigated DAC-PtM scenario

Input	Scenarios applied to	Assumptions	LCI data	Ref.
Water feed for electrolysers	All investigated scenarios: • Onshore wind, • Offshore wind, • Grid electricity	Water completely softened for industrial applications (including removal of Ca, Mg, and other metal cations in hard water), taking a global average.	0.69 g_{CO_2eq}/kg$_{water}$	[76, 77]
Catalyst	All investigated scenarios: • Onshore wind, • Offshore wind, • Grid electricity	The catalyst, comprising copper and zinc oxide on alumina support, is approximated as 70% copper (from sulfide ore) and 30% zinc, taking a global average for each.	1131 g_{CO_2eq}/kg$_{Cu}$ 2737 g_{CO_2eq}/kg$_{Zn}$	[76, 77]
Onshore wind power	Onshore wind scenarios	Global average for high-voltage electricity of grid-connected onshore wind power plants with a capacity above 3 MW	11.0 kg$_{CO_2eq}$/MWh	[69–72]
Offshore wind power	Offshore wind scenarios	Global average for high-voltage electricity of grid-connected offshore wind power plants with a capacity above 3 MW	25.0 kg$_{CO_2eq}$/MWh	[72–76]
European grid electricity	Grid-powered scenario	From high-voltage energy mix, excluding Switzerland	392 kg$_{CO_2eq}$/MWh	[76, 77]
Brazilian grid electricity	Grid-powered scenario	For a 2021 energy mix, using Ecoinvent [77] for the GWP associated with each power source.	155 kg$_{CO_2eq}$/MWh	[77, 79]
Chinese grid electricity	Grid-powered scenario	Averaging, the energy mixes of 2020 [81] and 2022 [82], taken across the entirety of mainland China.	578 kg$_{CO_2eq}$/MWh	[81, 82]
Battery storage	All investigated scenarios: • Onshore wind, • Offshore wind, • Grid electricity	Li-ion battery cell with a capacity of 209 Wh/kg$_{cell}$ and a lifetime of 15 years	72,944 kg$_{CO_2eq}$/MWh	[77]

Table 13: Breakdown of life cycle GWP results by input for the investigated wind-powered scenarios. All tabulated values are in GWP units of kg_{CO_2eq}/t_{MeOH}.

		Strategy 1			Strategy 2		
		Base	Optim.	Pessim.	Base	Optim.	Pessim.
	Electrolysis	126.4	105.8	157.6	109.5	93.7	148.3
	DAC	28.3	2.6	42.9	24.5	2.3	40.4
	CO_2 Comp.	13.3	11.5	18.1	11.4	9.9	17.0
	Non-CO_2 Comp.	2.4	1.0	3.4	2.1	0.9	3.1
Onshore	Heating	8.7	0.0	10.3	7.4	0.0	8.3
wind	Pumping and RO	0.1	0.1	0.1	0.1	0.1	0.1
	Water for electrolysis	0.6	0.5	0.7	2.7	2.2	3.0
	Cooling water	0.0	0.0	0.0	0.0	0.0	0.0
	Catalyst	0.3	0.0	1.3	0.3	0.1	2.7
	Batteries	32.6	3.9	133.1	81.2	5.8	87.2
	CO_2 emission	25.8	19.2	32.1	25.8	19.2	32.1
	CO_2 credit	-1,374.0	-1,374.0	-1,374.0	-1,374.0	-1,374.0	-1,374.0
	Absolute GWP	**-1,135.6**	**-1,229.3**	**-974.5**	**-1,109.0**	**-1,239.8**	**-1,031.9**
	Electrolysis	241.3	203.0	300.4	217.3	186.6	293.8
	DAC	53.9	5.0	81.8	48.7	4.6	80.0
	CO_2 Comp.	25.4	22.1	34.5	22.5	19.7	33.7
	Non-CO_2 Comp.	4.6	1.9	6.4	4.2	1.7	6.2
Offshore	Heating	16.6	0.0	19.5	14.7	0.0	16.7
wind	Pumping and RO	0.2	0.1	0.2	0.1	0.1	0.2
	Water for electrolysis	2.4	2.1	2.8	2.7	2.2	3.1
	Cooling water	0.0	0.0	0.0	0.0	0.0	0.0
	Catalyst	0.4	0.0	3.2	0.3	0.0	2.7
	Batteries	33.7	4.2	134.4	73.7	5.1	144.4
	CO_2 emission	25.8	19.2	32.1	25.8	19.2	32.1
	CO_2 credit	-1,374.0	-1,374.0	-1,374.0	-1,374.0	-1,374.0	-1,374.0
	Absolute GWP	**-969.8**	**-1,116.3**	**-758.8**	**-964.0**	**-1,134.8**	**-761.1**

Table 14: Breakdown of life cycle GWP results by input for the grid electricity case, under the three different grid energy mixes investigated: European, Brazilian, and Chinese. All tabulated values are in GWP units of kg_{CO_2eq}/t_{MeOH}.

	Grid electricity, Europe			Grid electricity, Brazil			Grid electricity, China		
	Base	Optim.	Pessim.	Base	Optim.	Pessim.	Base	Optim.	Pessim.
Electrolysis	3818.3	2,876.0	4,828.3	1,771.9	1,330.5	2,240.7	6,607.6	4,961.4	8,355.6
DAC	860.1	70.4	1,324.6	399.1	32.7	614.7	1,488.4	121.8	2,292.3
CO_2 Compression	388.0	296.2	535.8	180.0	137.5	248.7	671.4	512.6	927.3
Non-CO_2 Compression	72.2	26.4	93.0	33.5	12.3	43.2	125.0	45.7	160.9
Heating	206.0	0.0	222.0	95.6	0.0	103.0	365.5	0.0	384.3
Pumping and RO	2.1	1.3	2.6	1.0	0.6	1.2	3.6	2.3	4.4
Water for electrolysis	0.4	0.4	0.5	0.4	0.4	0.5	0.4	0.4	0.5
Cooling water	0.0	0.0	0.0	0.0	0.0	0.0	0.0	0.0	0.0
Catalyst	0.2	0.0	1.8	0.2	0.0	1.8	0.2	0.0	1.8
Batteries	0.0	0.0	0.0	0.0	0.0	0.0	0.0	0.0	0.0
CO_2 emission	25.8	19.2	32.1	25.8	19.2	32.1	25.8	19.2	32.1
CO_2 credit	-1,374.0	-1,374.0	-1,374.0	-1,374.0	-1,374.0	-1,374.0	-1,374.0	-1,374.0	-1,374.0
Absolute GWP	**3,999.1**	**1,906.9**	**5,666.7**	**1,133.7**	**159.1**	**1,911.8**	**7,905.0**	**4,289.4**	**10,785.1**

15 Location-specific DAC-PtM optimisation

15.1 Optimisation procedure

The two selected locations – Alice Springs in Australia, and in the North Sea – both delivered among the highest $\overline{CF}_{\text{plant}}$ values for onshore and offshore sites, respectively (**Tab. 5**), making them promising locations at which to consider further optimisation of DAC-PtM. Furthermore, the high quality of data available for the cost and life cycle emissions of wind power at each location – unlike other promising sites such as the Caribbean Sea off the coast of Venezuela – enables the site-specific modelling. However, besides the costs and life cycle impacts of wind power, as well as the local costs and carbon intensity of grid electricity, we took all other plant parameters to be the same as our global analysis under the base, optimistic, and pessimistic cases (**Tabs. 9-8**).

   In undertaking the site-specific modelling, we firstly optimised the dynamic operation of DAC-PtM at each site, namely minimising the size (and cost burden) of reserve storage. Specifically, the storage size at each site was reduced until the plant was just able to achieve continuous operation from 2016 to 2020 without emptying the storage levels, which was verified by using the wind speed data to continuously track the daily storage level at each site. In performing the optimisation, we also relaxed the operability limits of the reactors to enable operation down to 80% load. The revised $\overline{CF}_{\text{plant}}$, alongside storage requirement, was estimated under this framework for both Strategies 1 and 2; additionally, the case of a single reactor was also considered when allowing for the more the flexible operation. The site-specific tracking of storage levels was also used to revise the available electricity surplus at each site – *i.e.* whenever the storage level for a site was full, any electricity above that required to run DAC-PtM was added to the available electricity surplus. Finally, the sizing of reserve storage was adjusted to remove any battery storage for the surplus electricity.

15.2 Storage levels after optimisation

The daily tracking of storage levels shown in **Fig. 7** assumed the storage began in 2016 half-full, with each subsequent year beginning at the same level at which the other finished – *i.e.* the storage level at the end of December 2016 became the starting level for January 1 2017 *et cetera*. The fact the storage does not run empty across 2016-2020 therefore confirms the ability to achieve year-to-year cyclic operation of wind-powered DAC-PtM with the support of reserve storage.

   The tracking of storage levels also emphasises that reliance upon storage in the multi-reactor configuration predominantly takes the form of short-lived periods, shown by the sharp troughs in storage level in **Fig. 7a, b, d** and **e**, whereas the single, large reactor results in sustained periods of heavy reliance upon storage (**Fig. 7c, f**).
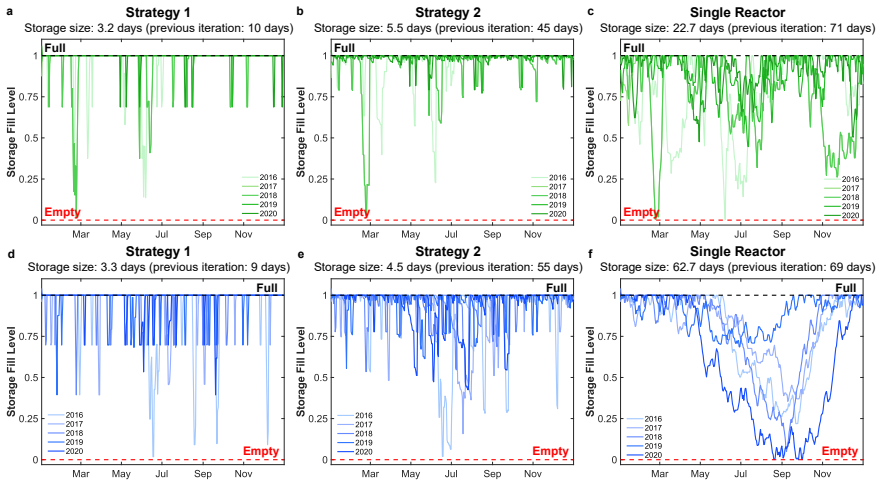
Fig. 7: The daily storage levels, determined continuously over the five-year period 2016-2020, after optimisation of the reserve storage size for DAC-PtM under the following circumstances: **a** Strategy 1, **b** Strategy 2, **c** a single, large reactor – all reliant upon an onshore wind farm sited at Alice Springs in Australia – **d** Strategy 1, **e** Strategy 2, **f** a single, large reactor — instead utilising power form an offshore wind farm in the North Sea off the UK Coast.

15.3 Wind power costs and life cycle inventory data for the North Sea

The specific location chosen for the North Sea windfarm lies approximately 300 km Northeast of Teeside: a similar location to the proposed Dogger Bank and Hornsea wind farms under construction to cumulatively deliver of the order 10 GW in nameplate capacity [83]. The site delivers a 5-year average wind farm capacity factor of 58.6%, which is held the same across the base, optimistic, and pessimistic cases. Hence, the required size of the wind farm is 133 MW in the base case, 86 MW in the optimistic, and 165 MW in the pessimistic.

In general, the cost of offshore wind is very high within Great Britain – sometimes exceeding the pessimistic cost estimates applied within the broader cost analysis across the globally-averaged sites. Work by Higgins and Foley [84] analysed the installation cost of offshore wind-farm installations in Great Britain up to 2013, by which point the 500 MW Gabbard was furthest from shore (around 30 km) at an installation cost of £2,600/kW (∼$3,300/kW adjusting for foreign exchange and inflation). Subsequent work by Aldersley-Williams *et al.* [85] estimated costs of £2,100/kW (∼$2,700/kW) for the Dudgeon wind farm, erected at a similar distance from shore. Both reports anticipated elevated costs for installation of wind farms further out to sea, requiring foundations in deeper waters.

Available data on the costs of the incomplete Dogger Bank and Hornsea wind farms (at *ca.* 300 km from the shoreline) remain speculative. Mytilinou

and Kolios [83] were able to investigate the effect of wind farm layouts upon both anticipated CAPEX and OPEX, yielding an optimised CAPEX estimate of £4,100/kW ($5,200/kW); however, estimated installation costs could be closer to £5,000/kW (∼$6,350/kW) for a wind farm of order 100 MW size, comparable to that proposed in the work here. Combining both existing and prospective cost data, Higgins and Foley [84] present an estimate for the scaling of wind farm costs according to (1) distance from shore, and (2) the number of turbines within the farm. Assuming installed wind turbine sizes of 6 MW, the wind farm requires either 22 (base), 14 (optimistic), or 28 (pessimistic) wind turbines at 300 km from the shore. Scaling the cost of the Gabbard farm (£2,600/kW) according to the Higgins and Foley methodology yields an estimated installation cost in the range £3,300 to 3,800/kW (∼$4,200-4,900/kW) – below the estimates of Mytilinou and Kolios.

The optimised OPEX of the Dogger Bank and Hornsea farms was estimated by Mytilinou and Kolios [83] as around £26.0/MWh(∼$33.6/MWh), but with the potential for costs of around £50/MWh (∼$63.5/MWh) at a scale of windfarm comparable to that required here. In general, European offshore wind farms are reported to require OPEX of between $27/MWh and $48/MWh [37].

The revised wind farm costs specific to the North Sea site are summarised below in **Tab. 15**. The span of costs are deemed representative of realistically attainable installation costs between the time period of now and 2030, for an offshore site situated far out in the North Sea (300 km from shore) as considered here.

Table 15: The capital and operating costs applied in the site-specific modelling of offshore wind power in the North Sea.

	Base	Optimistic	Pessimistic
Nameplate Capacity [MW]	133	86	165
Installed cost [million $]	693	424	1,050
Normalised cost [$/kW]	5,210	4,930	6,350
Operating costs [$/MWh]	33.6	27	63.5

For the sale of surplus electricity from the North Sea wind farm, we took current wholesale prices for renewable power in the UK, which are determined *via* the Contracts for Difference (CfD) scheme, wherein proposed projects enter an auction system for a contractually fixed price for the sale of generated electricity into the National Grid. In the most recent round [86], an average price of £52/MWh ($70/MWh) was agreed for renewable power projects to be delivered by 2030. We assume, therefore, that surplus electricity from the North Sea site is sold to the grid at $70/MWh across all three optimism cases. It is of moment, however, that no offshore wind projects participated in the recent auction round as they were deemed unviable at the agreed sale price.

To compare wind-powered DAC-PtM against utilising the local grid electricity, we also took UK prices for grid electricity, which are subject to fluctuations, as evidenced by the wholesale price ranging from during which the wholesale price ranged from £40/MWh ($51/MWh) up to £58/MWh ($74/MWh) in the years 2016 to 2021, before spiking at £200/MWh ($254/MWh) in 2022 and subsequently falling to £95/MWh ($121/MWh) in 2023 [87]. We assumed a similar a range of prices could be encountered by a chemical plant purchasing grid electricity from 2030 onwards: the base case assumes purchase of UK grid electricity at $85/MWh, falling to $50/MWh in the optimistic case and rising to $125/MWh in the pessimistic case.

For the life cycle analysis of the North Sea offshore wind farm, studies have reported the global warming potential to range from 15-32 kg_{CO_2eq}/MWh of electricity [88–90]. The distance of the wind farm from the shore affects emissions during the manufacturing, installation, and decommissioning phases, while also proportionally increasing emissions from the operation and maintenance (O&M) phase due to longer export cables and transit times for installation and decommissioning. Here, we estimate the carbon intensity of the GB North Sea offshore wind farm at 35 kg_{CO_2eq}/MWh by linearly increasing the contribution of O&M, compared to the 20 kg_{CO_2eq}/MWh value reported for a distance of 170 km [88]. To compare the GWP North Sea wind-powered DAC-PtM against utilising grid power, we took a carbon intensity of 210 kg_{CO_2eq}/MWh for the UK grid in 2023 [91]. All the LCI data used specific to the North Sea site are summarised in **Tab. 16**.

Table 16: Life cycle inventory (LCI) of emission factors and assumptions for the North Sea

Input	Scenarios applied to	Assumptions	LCI data	Ref.
Water feed to the electrolysers	All investigated scenarios: • Offshore wind, • Single reactor, • UK grid power	Water completely softened for industrial applications (including removal of Ca, Mg, and other metal cations in hard water), modelled for Europe	0.37 g_{CO_2eq}/kg$_{water}$	[76, 77]
Offshore wind power	UK Offshore wind	High-voltage electricity of grid-connected offshore wind farm in the North Sea, with a capacity above 3 MW at a distance from shore of 300 km	35 kg_{CO_2eq}/MWh	[88]
UK grid electricity	UK grid power	High-voltage electricity mix in the UK for 2023	210 kg_{CO_2eq}/MWh	[91]

15.4 Wind farm installation costs and life cycle inventory data for Alice Springs

The proposed wind farm location in Australia, near Alice Springs in the Northern Territory, lies near the centre of the country, delivering a 5-year average capacity factor of 36.5%, leading to required wind farm sizes of 218 MW under the base case, 141 MW in the optimistic case, and 271 MW in the pessimistic case. In a study on levelised electricity costs across Australia, Evans *et al.* [92] reported an installation cost of \$2,530/kW, around the pessimistic case estimate applied in the global-average modelling. Sovocol *et al.* [53] undertook a worldwide survey of installed wind farm costs. Of the Australian sites considered up to 2013, installation costs ranged from \$2,145/kW to \$2,645/kW for farms of a comparable size to that required here. Two recent technical reports [93, 94] estimated the installation cost for a 300 MW capacity onshore wind farm as \$1,850/kW in 2021, rising to \$2,500 in 2022. The OPEX of an Australian onshore wind farm was estimated as \$13.7/MWh [92]. No further information is available, and so we take an assumed 50% variation between the optimistic and pessimistic cases, with resulting costs that lie at the very upper-end of the OPEX in the global analysis (**Tab. 8**). The wind-farm costs are summarised in **Tab. 17**.

Table 17: The capital and operating costs applied in the site-specific modelling of onshore wind power at Alice Springs in Australia.

	Base	Optimistic	Pessimistic
Nameplate Capacity [MW]	218	141	271
Installed cost [million \$]	563	263	743
Normalised cost [\$/kW]	2,500	1,850	2,650
Operating costs [\$/MWh]	13.7	6.9	20.6

For the sale of surplus or purchase of grid electricity, we considered the wholesale spot price of electricity in Australia which varies between regions, with plans to implement a CfD scheme for the sale of renewable electricity. We assume, therefore, that surplus renewable power is sold at some time-averaged wholesale price, whereas the grid purchase price is subject to fluctuations. Data for the Northern Territory are not reported, although the neighbouring region of Queensland had an average wholesale price of AU\$75/MWh (\$50/MWh) between 2016 and 2021, peaking at AU\$344/MWh (\$226/MWh) in 2022. The average for the period 2022-2023 was AU\$174/MWh (\$115/MWh) [95]. Given the trend shown in the UK of CfD prices lying below grid wholesale prices, we take an estimate of \$40/MWh as the sale price for all surplus electricity, whereas the grid purchase price was taken as \$50/MWh, \$40/MWh, and \$115/MWh in the base, optimistic, and pessimistic cases, respectively.

For the emissions associated with construction of an onshore wind farm at Alice Springs, we used the LCI value from Ecoinvent database for Australia [77], which assumes a 2 MW farm capacity and includes both the embedded emissions of construction and the GWP associated with operation and maintenance of the wind farm. The value used is an average for Australia in general, rather than specific to Alice Springs, leaving some uncertainty about the true associated emissions for a wind farm at the exact location considered in our analysis. A full summary of the LCI values used, specific to Australia, is given in **Tab. 18** below.

Table 18: Life cycle inventory (LCI) of emission factors and assumptions for Alice Springs

Input	Scenerios applied to	Assumptions	LCI data	Ref.
Onshore wind power	Australian Onshore wind	High-voltage electricity of grid-connected offshore wind power plants with a capacity above 3 MW	21.4 kg_{CO_2eq}/MWh	[77]
Australian grid electricity	Grid electricity	High voltage electricity in Australia in 2023	600 kg_{CO_2eq}/MWh	[96]

15.5 The selling prices of methanol and effective costs of net CO_2 capture

Combining the site-specific cost analyses and life cycle assessments, according to **Eq. 6**, yielded the effective CO_2 capture costs tabulated in **Tab. 19**.

Table 19: The selling prices of MeOH, GWP, and the effective cost of CO_2 capture for wind-powered DAC-PtM after site-specific optimisation and modelling for the Alice Springs (Australia) and North Sea (UK) wind farm locations.

		MeOH Selling Price [$/t_{MeOH}]			GWP [kg_{CO_2eq}/t_{MeOH}]			CO_2 capture cost [$/t_{CO_2eq}]		
		Base	Optimistic	Pessimistic	Base	Optimistic	Pessimistic	Base	Optimistic	Pessimistic
Alice Springs	Strategy 1	1,925	788	3,453	-986	-1,111	-830	1,953	710	4,163
	Strategy 2	1,800	746	3,161	-1,024	-1,139	-870	1,758	655	3,634
	Single Reactor	2,479	785	4,170	-970	-1112	-925	2,556	705	4,507
North Sea	Strategy 1	3,023	1,433	6,637	-779	-967	-525	3,882	1,481	12,646
	Strategy 2	2,407	1,122	4,890	-839	-1,013	-585	2,869	1,108	8,358
	Single Reactor	3,469	1,650	6,233	-736	-963	-669	4,710	1,714	9,314

16 Reactor design considerations for dynamic operation

Water-cooling, as we consider here and shown in **Fig. 8a**, is a common strategy to control temperature in methanol reactors [27], and has a safety advantage

over the gas-cooling alternative (shown in **Fig. 8b**), as the reactor temperature control is independent of whether feed gas is flowing to the reactor. The temperature of a water-cooled reactor can be maintained at a safe level after shut-down, when feed is no longer flowing to the reactor.
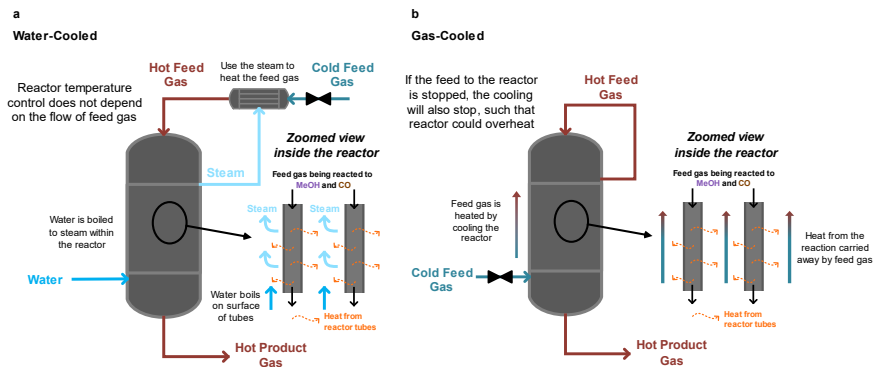

Fig. 8: Cooling configurations for reactors used to produce methanol. **a** Schematic of a water-cooled methanol reactor. The reactor cooling, through boiling water to steam, can be continued even after the flow of feed gas to the reactor has been stopped. **b** Schematic of a gas-cooled methanol reactor. The temperature control of the reactor is achieved by integrating the reactor cooling to the pre-heating of feed gas. Therefore, if the feed gas flow is stopped, the ability to control reactor temperature diminishes.

References

[1] Fogel, S., Unger, S. & Hampel, U. Dynamic system modeling and simulation of a power-to-methanol process based on proton-conducting tubular solid oxide cells. *Energy Conversion and Management* **300**, 117970 (2024). https://doi.org/10.1016/j.enconman.2023.117970 .

[2] Van Antwerpen, J. *et al.* A model for assessing pathways to integrate intermittent renewable energy for e-methanol production. *International Journal of Hydrogen Energy* (2023). https://doi.org/10.1016/j.ijhydene.2023.04.177 .

[3] Zheng, N., Zhu, H., Xiao, G., Ni, M. & Xu, H. Dynamic-cycle simulation of power-to-methanol-to-power system with reversible solid oxide cells: Multi-physics and techno-economic analysis. *Energy Conversion and Management* **294**, 117573 (2023). https://doi.org/10.1016/j.enconman.2023.117573 .

[4] Moioli, E. & Schildhauer, T. Eco-techno-economic analysis of methanol production from biogas and Power-to-X. *Industrial & Engineering Chemistry Research* **61** (21), 7335–7348 (2022). https://doi.org/10.1021/acs.iecr.1c04682 .

[5] Sollai, S., Porcu, A., Tola, V., Ferrara, F. & Pettinau, A. Renewable methanol production from green hydrogen and captured CO_2: A techno-economic assessment. *Journal of CO_2 Utilization* **68**, 102345 (2023). https://doi.org/10.1016/j.jcou.2022.102345 .

[6] Zheng, Y., You, S., Li, X., Bindner, H. W. & Münster, M. Data-driven robust optimization for optimal scheduling of power to methanol. *Energy Conversion and Management* **256**, 115338 (2022). https://doi.org/10.1016/j.enconman.2022.115338 .

[7] Cui, X., Kær, S. K. & Nielsen, M. P. Energy analysis and surrogate modeling for the green methanol production under dynamic operating conditions. *Fuel* **307**, 121924 (2022). https://doi.org/10.1016/j.fuel.2021.121924 .

[8] Chen, C. & Yang, A. Power-to-methanol: The role of process flexibility in the integration of variable renewable energy into chemical production. *Energy Conversion and Management* **228**, 113673 (2021). https://doi.org/10.1016/j.enconman.2020.113673 .

[9] Bos, M., Kersten, S. & Brilman, D. Wind power to methanol: Renewable methanol production using electricity, electrolysis of water and CO_2 air capture. *Applied energy* **264**, 114672 (2020). https://doi.org/10.1016/j.apenergy.2020.114672 .

[10] Daggash, H. A. *et al.* Closing the carbon cycle to maximise climate change mitigation: power-to-methanol *vs* power-to-direct air capture. *Sustainable Energy & Fuels* **2** (6), 1153–1169 (2018). https://doi.org/10.1039/C8SE00061A .

[11] Gutsch, M. & Leker, J. Co-assessment of costs and environmental impacts for off-grid direct air carbon capture and storage systems. *Communications Engineering* **3** (1), 14 (2024). https://doi.org/10.1038/s44172-023-00152-6 .

[12] Breyer, C., Fasihi, M. & Aghahosseini, A. Carbon dioxide direct air capture for effective climate change mitigation based on renewable electricity: a new type of energy system sector coupling. *Mitigation and Adaptation Strategies for Global Change* **25**, 43–65 (2020). https://doi.org/10.1007/s11027-019-9847-y .

[13] Pratschner, S., Hammerschmid, M., Müller, S. & Winter, F. Off-grid vs. grid-based: Techno-economic assessment of a power-to-liquid plant combining solid-oxide electrolysis and Fischer-Tropsch synthesis. *Chemical Engineering Journal* **481**, 148413 (2024). https://doi.org/10.1016/j.cej.2023.148413 .

[14] Loewert, M., Riedinger, M. & Pfeifer, P. Dynamically operated fischer–tropsch synthesis in ptl—part 2: Coping with real pv profiles. *ChemEngineering* **4** (2) (2020). https://doi.org/10.3390/chemengineering4020027 .

[15] Shirazi, A., Rahbari, A., Asselineau, C.-A. & Pye, J. A solar fuel plant via supercritical water gasification integrated with Fischer-Tropsch synthesis: System-level dynamic simulation and optimisation. *Energy Conversion and Management* **192**, 71–87 (2019). https://doi.org/10.1016/j.enconman.2019.04.008 .

[16] Giglio, E., Pirone, R. & Bensaid, S. Dynamic modelling of methanation reactors during start-up and regulation in intermittent power-to-gas applications. *Renewable Energy* **170**, 1040–1051 (2021). https://doi.org/10.1016/j.renene.2021.01.153 .

[17] Gorre, J., Ruoss, F., Karjunen, H., Schaffert, J. & Tynjälä, T. Cost benefits of optimizing hydrogen storage and methanation capacities for power-to-gas plants in dynamic operation. *Applied Energy* **257**, 113967 (2020). https://doi.org/10.1016/j.apenergy.2019.113967 .

[18] Mock, M. *et al.* Dynamic operation for the effective use of green hydrogen in power-to-x value chains. *Computer Aided Chemical Engineering* **52**, 1267–1272 (2023). https://doi.org/10.1016/B978-0-443-15274-0.50202-X .

[19] Verleysen, K., Parente, A. & Contino, F. How does a resilient, flexible ammonia process look? Robust design optimization of a Haber-Bosch process with optimal dynamic control powered by wind. *Proceedings of the Combustion Institute* **39** (4), 5511–5520 (2023). https://doi.org/10.1016/j.proci.2022.06.027 .

[20] Ishaq, H. & Dincer, I. Dynamic modelling of a solar hydrogen system for power and ammonia production. *International Journal of Hydrogen Energy* **46** (27), 13985–14004 (2021). https://doi.org/10.1016/j.ijhydene.2021.01.201 .

[21] Ikäheimo, J., Kiviluoma, J., Weiss, R. & Holttinen, H. Power-to-ammonia in future North European 100% renewable power and heat system. *International Journal of Hydrogen Energy* **43** (36), 17295–17308 (2018). https://doi.org/10.1016/j.ijhydene.2018.06.121 .

[22] Cheema, I. I. & Krewer, U. Operating envelope of haber-bosch process design for power-to-ammonia. *RSC Advances* **8** (61), 34926–34936 (2018). https://doi.org/10.1039/C8RA06821F .

[23] Cole, W. J. & Frazier, A. Cost projections for utility-scale battery storage. Tech. Rep., National Renewable Energy Laboratory (NREL) (2019). NREL/TP-6A20-79236.

[24] Baldwin, D. Development of high pressure hydrogen storage tank for storage and gaseous truck delivery. Tech. Rep., Hexagon Lincoln LLC, Lincoln (2017).

[25] Liu, Z., Yang, X., Jia, W., Li, H. & Yang, X. Justification of CO_2 as the working fluid for a compressed gas energy storage system. *Journal of Energy Storage* **27**, 101132 (2020). https://doi.org/10.1016/j.est.2019.101132 .

[26] de Klerk, A. *Future Energy*, Ch. Transport fuel: Biomass-, coal-, gas-and waste-to-liquids processes, 199–226 (Elsevier, 2020).

[27] Bozzano, G. & Manenti, F. Efficient methanol synthesis: Perspectives, technologies and optimization strategies. *Progress in Energy and Combustion Science* **56**, 71–105 (2016). https://doi.org/10.1016/j.pecs.2016.06.001 .

[28] Mbatha, S. *et al.* Power-to-methanol process: a review of electrolysis, methanol catalysts, kinetics, reactor designs and modelling, process integration, optimisation, and techno-economics. *Sustainable Energy & Fuels* **5** (14), 3490–3569 (2021). https://doi.org/10.1039/D1SE00635E .

[29] Ulrich, G. D. & Vasudevan, P. T. How to estimate utility costs. *Chemical Engineering* **113** (4), 66–69 (2006) .

[30] Burgess, D. R.   in *NIST chemistry webbook: NIST standard reference database number 69* (eds Linstrom, P. & Mallard, W.) Ch. Thermochemical Data (National Institute of Standards and Technology (NIST)).

[31] Matsoukas, T. *Fundamentals of Chemical Engineering Thermodynamics* (Pearson, 2012).

[32] Bussche, K. & Froment, G. A steady-state kinetic model for methanol synthesis and the water gas shift reaction on a commercial $Cu/ZnO/Al_2O_3$ catalyst. *Journal of Catalysis* **161** (1), 1–10 (1996). https://doi.org/10.1006/jcat.1996.0156 .

[33] Hendren, N. & Baumann, R.   McCabe-Thiele method for methanol/water separation (2016). URL demonstrations.wolfram.com/McCabeThieleMethodForMethanolWaterSeparation/. Accessed March 29, 2022.

[34] Towler, G. & Sinnott, R.   *Chemical engineering design: principles, practice and economics of plant and process design* 3 edn (Butterworth-Heinemann, 2021).

[35] Prašnikar, A., Pavlišič, A., Ruiz-Zepeda, F., Kovač, J. & Likozar, B. Mechanisms of copper-based catalyst deactivation during CO_2 reduction to methanol. *Industrial & Engineering Chemistry Research* **58** (29), 13021–13029 (2019). https://doi.org/10.1021/acs.iecr.9b01898 .

[36] Dieterich, V., Buttler, A., Hanel, A., Spliethoff, H. & Fendt, S. Power-to-liquid *via* synthesis of methanol, DME or Fischer–Tropsch-fuels: a review. *Energy & Environmental Science* **13**, 3207–3252 (2020). https://doi.org/10.1039/D0EE01187H .

[37] International Renewable Energy Agency (IRENA).   Renewable energy technologies: Cost analysis series: Wind power (2012).

[38] Wiser, R., Bolinger, M. & Lantz, E.   Assessing wind power operating costs in the united states: Results from a survey of wind industry experts. *Renewable Energy Focus* **30**, 46–57 (2019). https://doi.org/10.1016/j.ref.2019.05.003 .

[39] Ederer, N. Evaluating capital and operating cost efficiency of offshore wind farms: A dea approach. *Renewable and Sustainable Energy Reviews* **42**, 1034–1046 (2015). https://doi.org/10.1016/j.rser.2014.10.071 .

[40] Shafiee, M., Brennan, F. & Espinosa, I. A. A parametric whole life cost model for offshore wind farms. *The International Journal of Life Cycle Assessment* **21**, 961–975 (2016). https://doi.org/10.1007/s11367-016-1075-z .

[41] Judge, F. *et al.* A lifecycle financial analysis model for offshore wind farms. *Renewable and Sustainable Energy Reviews* **103**, 370–383 (2019). https://doi.org/10.1016/j.rser.2018.12.045 .

[42] Kumar, S. S. & Himabindu, V. Hydrogen production by PEM water electrolysis–a review. *Materials Science for Energy Technologies* **2** (3), 442–454 (2019). https://doi.org/10.1016/j.mset.2019.03.002 .

[43] Shayesteh, A. A., Koohshekan, O., Ghasemi, A., Nemati, M. & Mokhtari, H. Determination of the orc-ro system optimum parameters based on 4e analysis; water–energy-environment nexus. *Energy Conversion and Management* **183**, 772–790 (2019). https://doi.org/10.1016/j.enconman.2018.12.119 .

[44] Fasihi, M., Efimova, O. & Breyer, C. Techno-economic assessment of CO_2 direct air capture plants. *Journal of cleaner production* **224**, 957–980 (2019). https://doi.org/10.1016/j.jclepro.2019.03.086 .

[45] Sabatino, F. *et al.* A comparative energy and costs assessment and optimization for direct air capture technologies. *Joule* **5** (8), 2047–2076 (2021). https://doi.org/10.1016/j.joule.2021.05.023 .

[46] Rahman, M., Ibrahim, T. K. & Abdalla, A. N. Thermodynamic performance analysis of gas-turbine power-plant. *International journal of physical sciences* **6** (14), 3539–3550 (2011). https://doi.org/10.5897/IJPS11.272 .

[47] Sarp, S., Hernandez, S. G., Chen, C. & Sheehan, S. W. Alcohol production from carbon dioxide: methanol as a fuel and chemical feedstock. *Joule* **5** (1), 59–76 (2021). https://doi.org/10.1016/j.joule.2020.11.005 .

[48] Nyári, J., Magdeldin, M., Larmi, M., Järvinen, M. & Santasalo-Aarnio, A. Techno-economic barriers of an industrial-scale methanol CCU-plant. *Journal of CO_2 utilization* **39**, 101166 (2020). https://doi.org/10.1016/j.jcou.2020.101166 .

[49] Mignard, D. Correlating the chemical engineering plant cost index with macro-economic indicators. *Chemical Engineering Research and Design* **92** (2), 285–294 (2014). https://doi.org/10.1016/j.cherd.2013.07.022 .

[50] Jenkins, S.   2019 Chemical engineering plant cost index annual average (2020).   URL chemengonline.com/

2019-chemical-engineering-plant-cost-index-annual-average/.   Accessed 10 March 2022.

[51] Amirkhas, E., Bedi, R., Harley, S. & Lango, T. Methanol production in trinidad & tobago. Tech. Rep., University of California, Davis (2006).

[52] Bailey, M. P. Chemical engineering plant cost index (CEPCI). *Chemical Engineering* **121** (2), 68–69 (2014) .

[53] Sovacool, B. K., Enevoldsen, P., Koch, C. & Barthelmie, R. J. Cost performance and risk in the construction of offshore and onshore wind farms. *Wind Energy* **20** (5), 891–908 (2017). https://doi.org/10.1002/we.2069 .

[54] Gonzalez-Rodriguez, A. G. Review of offshore wind farm cost components. *Energy for Sustainable Development* **37**, 10–19 (2017). https://doi.org/10.1016/j.esd.2016.12.001 .

[55] Díaz, H. & Soares, C. G. Review of the current status, technology and future trends of offshore wind farms. *Ocean Engineering* **209**, 107381 (2020). https://doi.org/10.1016/j.oceaneng.2020.107381 .

[56] Saba, S. M., Müller, M., Robinius, M. & Stolten, D. The investment costs of electrolysis–a comparison of cost studies from the past 30 years. *International Journal of Hydrogen Energy* **43** (3), 1209–1223 (2018). https://doi.org/10.1016/j.ijhydene.2017.11.115 .

[57] Khan, M. H. A. *et al.* Designing optimal integrated electricity supply configurations for renewable hydrogen generation in australia. *IScience* **24** (6) (2021). https://doi.org/10.1016/j.isci.2021.102539 .

[58] Panah, P. G., Cui, X., Bornapour, M., Hooshmand, R.-A. & Guerrero, J. M. Marketability analysis of green hydrogen production in Denmark: Scale-up effects on grid-connected electrolysis. *International Journal of Hydrogen Energy* **47** (25), 12443–12455 (2022). https://doi.org/10.1016/j.ijhydene.2022.01.254 .

[59] Caldera, U. & Breyer, C. Learning curve for seawater reverse osmosis desalination plants: capital cost trend of the past, present, and future. *Water Resources Research* **53** (12), 10523–10538 (2017). https://doi.org/10.1002/2017WR021402 .

[60] Dorris, C. C., Lu, E., Park, S. & Toro, F. H. High-purity oxygen production using mixed ionic-electronic conducting sorbents. Tech. Rep., University of Pennsylvannia, LP Amina (2016).

[61] Taibi, E., Miranda, R., Carmo, M. & Blanco, H.   Green hydrogen cost reduction. Tech. Rep., Hydrogen Knowledge Centre, International Renewable Energy Agency (IRENA) (2020).

[62] Rennert, K. *et al.* Comprehensive evidence implies a higher social cost of CO_2. *Nature* 1–3 (2022). https://doi.org/10.1038/s41586-022-05224-9 .

[63] Li, J., Ma, X., Liu, H. & Zhang, X. Life cycle assessment and economic analysis of methanol production from coke oven gas compared with coal and natural gas routes. *Journal of Cleaner Production* **185**, 299–308 (2018). https://doi.org/10.1016/j.jclepro.2018.02.100 .

[64] Adnan, M. A. & Kibria, M. G.   Comparative techno-economic and life-cycle assessment of power-to-methanol synthesis pathways. *Applied Energy* **278**, 115614 (2020).   https://doi.org/10.1016/j.apenergy.2020.115614 .

[65] Lerner, A., Brear, M. J., Lacey, J. S., Gordon, R. L. & Webley, P. A. Life cycle analysis (LCA) of low emission methanol and di-methyl ether (DME) derived from natural gas. *Fuel* **220**, 871–878 (2018). https://doi.org/10.1016/j.fuel.2018.02.066 .

[66] Kajaste, R., Hurme, M. & Oinas, P. Methanol-managing greenhouse gas emissions in the production chain by optimizing the resource base. *Aims Energy* **6** (6), 1074–1102 (2018). https://doi.org/10.3934/energy.2018.6.1074 .

[67] Carbon footprint of methanol. Tech. Rep., Methanol institute (2022).

[68] Liu, Y. *et al.*   Comprehensive analysis of environmental impacts and energy consumption of biomass-to-methanol and coal-to-methanol via life cycle assessment. *Energy* **204**, 117961 (2020). https://doi.org/10.1016/j.energy.2020.117961 .

[69] Li, Q. *et al.*   Life cycle assessment and life cycle cost analysis of a 40 mw wind farm with consideration of the infrastructure. *Renewable and Sustainable Energy Reviews* **138**, 110499 (2021). https://doi.org/10.1016/j.rser.2020.110499 .

[70] Life cycle assessment of electricity production from an onshore V136-4.2 MW wind plant. Tech. Rep., Vestas (2022).

[71] Verma, S., Paul, A. R. & Haque, N. Selected environmental impact indicators assessment of wind energy in India using a life cycle assessment. *Energies* **15** (11), 3944 (2022). https://doi.org/10.3390/en15113944 .

[72] Bonou, A., Laurent, A. & Olsen, S. I. Life cycle assessment of onshore and offshore wind energy-from theory to application. *Applied Energy* **180**, 327–337 (2016). https://doi.org/10.1016/j.apenergy.2016.07.058 .

[73] Garcia-Teruel, A., Rinaldi, G., Thies, P. R., Johanning, L. & Jeffrey, H. Life cycle assessment of floating offshore wind farms: An evaluation of operation and maintenance. *Applied Energy* **307**, 118067 (2022). https://doi.org/10.1016/j.apenergy.2021.118067 .

[74] Kaldellis, J. & Apostolou, D. Life cycle energy and carbon footprint of offshore wind energy. Comparison with onshore counterpart. *Renewable Energy* **108**, 72–84 (2017). https://doi.org/10.1016/j.renene.2017.02.039 .

[75] Yang, J. *et al.* The life-cycle energy and environmental emissions of a typical offshore wind farm in China. *Journal of Cleaner Production* **180**, 316–324 (2018). https://doi.org/10.1016/j.jclepro.2018.01.082 .

[76] Oele, M. & Dolfing, R. Simapro (2019).

[77] Frischknecht, R. *et al.* The ecoinvent database: overview and methodological framework (7 pp). *The international journal of life cycle assessment* **10**, 3–9 (2005). https://doi.org/10.3929/ethz-b-000413470 .

[78] Scarlat, N., Prussi, M. & Padella, M. Quantification of the carbon intensity of electricity produced and used in europe. *Applied Energy* **305**, 117901 (2022). https://doi.org/10.1016/j.apenergy.2021.117901 .

[79] Barros, M. V., Piekarski, C. M. & De Francisco, A. C. Carbon footprint of electricity generation in Brazil: An analysis of the 2016–2026 period. *Energies* **11** (6), 1412 (2018). https://doi.org/10.3390/en11061412 .

[80] Climate Transparency. Brazil – climate transparency report: Comparing G20 action (2022). URL https://www.climate-transparency.org/wp-content/uploads/2022/10/CT2022-Brazil-Web.pdf. Accessed 07/09/2023.

[81] Zhang, X., Zhu, Q. & Zhang, X. Carbon emission intensity of final electricity consumption: Assessment and decomposition of regional power grids in China from 2005 to 2020. *Sustainability* **15** (13), 9946 (2023). https://doi.org/10.3390/su15139946 .

[82] Climate Transparency. China – climate transparency report: Comparing G20 action (2022). URL https://www.climate-transparency.org/wp-content/uploads/2022/10/CT2022-China-Web.pdf. Accessed 08/09/2023 .

[83] Mytilinou, V. & Kolios, A. J. Techno-economic optimisation of offshore wind farms based on life cycle cost analysis on the uk. *Renewable Energy* **132**, 439–454 (2019). https://doi.org/10.1016/j.renene.2018.07.146 .

[84] Higgins, P. & Foley, A. The evolution of offshore wind power in the united kingdom. *Renewable and sustainable energy reviews* **37**, 599–612 (2014). https://doi.org/10.1016/j.rser.2014.05.058 .

[85] Aldersey-Williams, J., Broadbent, I. D. & Strachan, P. A. Better estimates of lcoe from audited accounts – a new methodology with examples from united kingdom offshore wind and ccgt. *Energy Policy* **128**, 25–35 (2019). https://doi.org/10.1016/j.enpol.2018.12.044 .

[86] Watson, N. & Bolton, P. Contracts for difference. Tech. Rep., UK Government (2023).

[87] National Grid ESO data portal. URL https://www.nationalgrideso.com/data-portal. Accessed 29/01/2024.

[88] Reimers, B., Özdirik, B. & Kaltschmitt, M. Greenhouse gas emissions from electricity generated by offshore wind farms. *Renewable energy* **72**, 428–438 (2014). https://doi.org/10.1016/j.renene.2014.07.023 .

[89] Birkeland, C. *Assessing the life cycle environmental impacts of offshore wind power generation and power transmission in the North Sea.* Master's thesis, Institutt for energi-og prosessteknikk (2011).

[90] Wagner, H.-J. *et al.* Life cycle assessment of the offshore wind farm alpha ventus. *Energy* **36** (5), 2459–2464 (2011). https://doi.org/10.1016/j.energy.2011.01.036 .

[91] Department for Energy Security and Net Zero, UK Government. Green book supplementary guidance: Valuation of energy use and greenhouse gas emissions for appraisal (2023).

[92] Evans, J. P., Kay, M., Prasad, A. & Pitman, A. The resilience of australian wind energy to climate change. *Environmental Research Letters* **13** (2), 024014 (2018). https://doi.org/10.1088/1748-9326/aaa632 .

[93] Aurecon. 2021 costs and technical parameter review Australian energy market operator. Tech. Rep., Australian Energy Market Operator (2021).

[94] Aurecon. 2022 costs and technical parameter review Australian energy market operator. Tech. Rep., Australian Energy Market Operator (2022).

[95] Australian Energy Regulator. Monitoring performance and analysing trends. URL https://www.aer.gov.au/industry/wholesale/charts.

Accessed 30/01/2024.

[96] Department of Climate Change, Energy, the Environment and Water, Australian Government. Australia's emissions projections 2023 (2023).